UiT
THE ARCTIC
UNIVERSITY
OF NORWAY

Faculty of Science and Technology
Department of Physics and Technology

Sensitivity to pressure and methane of a cryptophane-A doped polymer

—
Martin Ingvaldsen
FYS-3900 Master's thesis in physics – December 2015

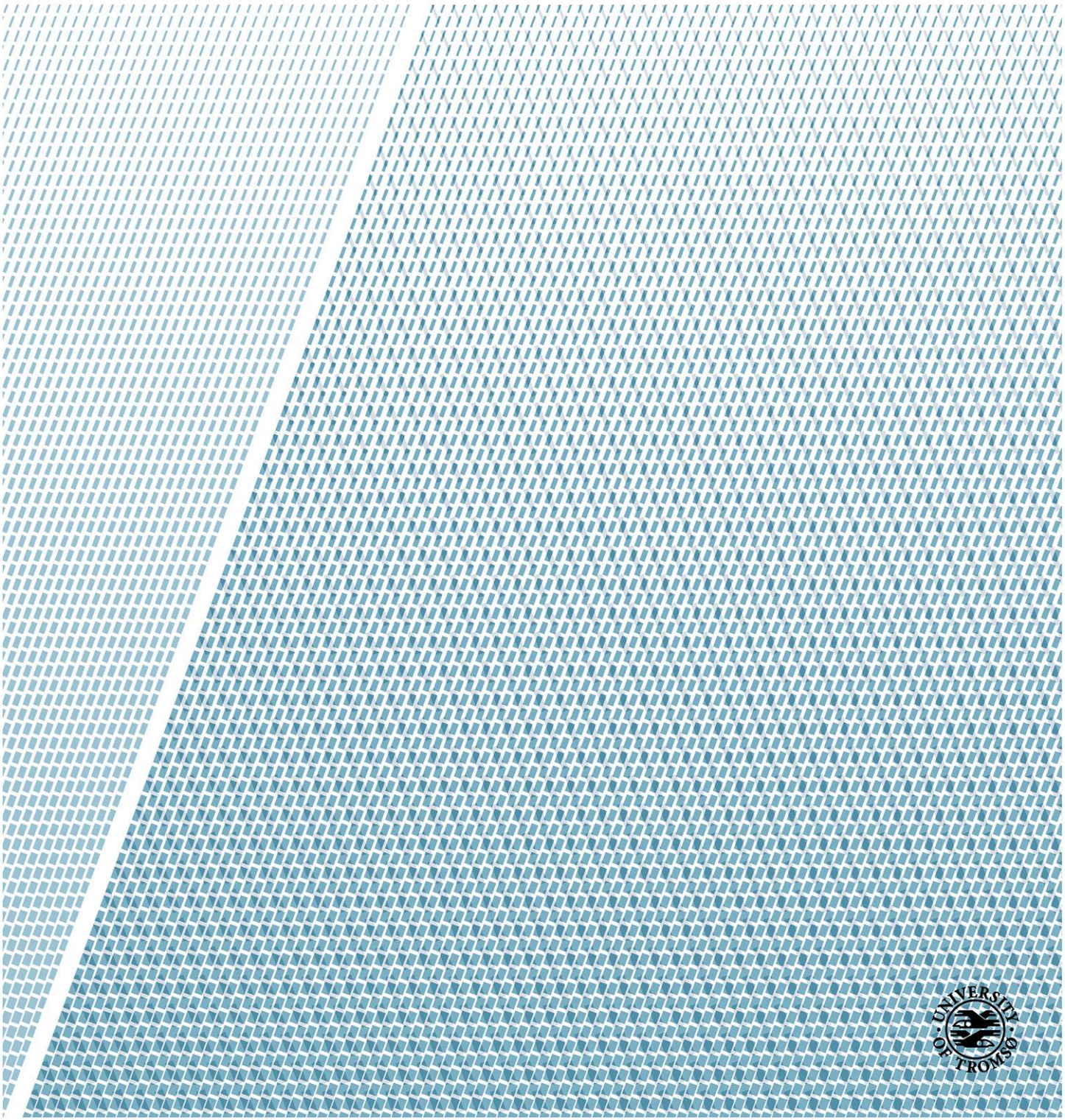

Abstract

The principle focus of this thesis is the characterization of an on-chip methane sensor based on a waveguide interferometer. It incorporates cryptophane-A molecules in the waveguide cladding to enhance sensitivity and selectivity towards methane.

First, the sensor was characterized for sensitivities to ambient conditions, in particular its temperature and pressure sensitivity. The measurement results show that a symmetric waveguide interferometer, with the same material on both arms, is almost insensitive to uniform changes in temperature and pressure. On the other hand, an asymmetric waveguide interferometer, with different materials on the arms, is highly temperature and pressure sensitive. However, numerical simulations revealed that a symmetric device can be sensitive to asymmetric heating of the top surface.

Second, the methane sensitivity of the sensor was tested with both pure polymer and polymer doped with cryptophane-A as the sensing medium. Using pure polymer resulted in a moderate sensitivity to methane, which linearly increased with pressure. While polymer doped with cryptophane-A resulted in more than 50-fold enhancement in sensitivity. Furthermore, the sensitivity was shown to be directly proportional to the concentration of cryptophane-A and increasing with pressure. A detection limit of 5 ppm was achieved, which is 1-2 orders of magnitude better than reported for comparable small and low-cost methane sensors.

As a greenhouse gas, methane has a high global warming potential and its atmospheric concentration has increased drastically over the past centuries. Hence, the interest in measuring and mapping the methane sources and atmospheric concentration has increased. The work in this thesis is paving

the way for a high sensitive methane sensor, but still low-cost and compact enough to be mounted on drones and employed in poorly accessibly areas.

Acknowledgements

I am sincerely thankful to my supervisor, Prof. Olav Gaute Hellesø, and my co-supervisor, Dr. Jana Jágerská, for their constructive comments, helpful guidance, countless discussions and constant support during my master thesis.

I also extend my gratitude to Dr. Firehun Tsige Dullo for his informative discussion, support and collaboration on experimental work for the project.

I would also like to thank Susan Lindecrantz for teaching me the lab procedures and including me in her measurements at the early stages of my master studies.

I am grateful to all members of optics group at University of Tromsø for the countless conversations and enlightening discussion on the project, both personally and during our optics meeting time.

I would like to thank four internship students who have been present here in Tromsø during the period of my thesis, and made my day simpler. I thank Clement Crouzet for his design and production of mechanical parts for the setup. Robin Chatel and Carolin Lueders for their work of developing and improving the LabVIEW programs used for measurement. And Gaëtan Floriach for his simulations of evanescent field distribution, homogeneous sensitivities and phase changes.

Further on I would like to thank the Department of Physics and Technology for the possibility to do my masters and working in a brand new lab and the Department of Chemistry for fabrication of Cryptophane-A.

Finally, I would like to thank my family and friends for their support in any respect during my years at the University of Tromsø.

Contents

Chapter 1

Introduction

1.1 Motivation

Methane (CH_4) has been studied for more than 200 years as an important atmospheric compound [1]. Since the pre-industrial times the atmospheric concentration of methane has increased by 250%, from 0.7 ppm to 1.8 ppm [2], and is estimated to be responsible for 15% to 22% of the greenhouse effect [3–5]. Combining this with the global warming potential of methane over the next 100 years being 34 times greater than the potential of carbon dioxide (CO_2) [6], the interest of following the methane concentration and emissions have increased in recent years. Aqueous environments, including oceans, wetlands, permafrost and methane clathrates have the potential to become major methane sources in a warmer climate [7]. Thus, quantifying the atmospheric methane concentration and emission sources is essential for the understanding of the global methane cycle [8]. The contributions of the remote sources are not precisely known due to their locations and lack of reliable measurements [9, 10]. Cheap and miniature sensors are available for methane sensing, but these suffer from long-term drift, limited sensitivity and cross-responsivity to other chemical species [11]. On the other side is traditional high-end laboratory equipment, which have high sensitivity (ppb level), can have high specificity to the chemical species and long-term stability, but are large, slow and expensive [12, 13]. The task of

quantifying the emissions from remote sources requires a low-cost, sensitive methane sensor, but still sufficiently small and robust enough to be carried by unmanned aerial vehicles (UAV) and operate in extreme weather conditions.

One approach to this problem might be the use of on-chip interferometers. On-chip interferometers are of small size and provide high sensitivity, proportional to optical path-length and indirectly to a range of physical, biological and chemical parameters. The use of interferometers have already been successfully used in optical trapping [14] and sensing of pressure, temperature, gases, DNA/RNA and other biological compounds [8, 15–21]. The disadvantage of using interferometers are their high sensitivity to ambient conditions and other parameters than the measurand. The Mach-Zehnder interferometer (MZI) is the most studied interferometer for evanescent field sensing [21, 22], with the advantage of using a reference arm that can reduce unwanted sensitivities. Special designs to give a high sensitivity that is independent of other parameters have been proven possible [23, 24].

A way of increasing the sensitivity and selectivity of the interferometer to a certain chemical species is the use of supra-molecular compounds called cryptophanes [25]. Cryptophanes form host cavities that can trap molecules of dimension fitting the cavity. The smallest of the cryptophanes, cryptophane-A, exhibits a strong affinity towards methane [26–28]. Hence, transparent films of Styrene-Acrylonitrile (SAN) can be doped with cryptophane-A and used as a sensitive cladding layer for optical refractive index sensors as the MZI [8, 19, 28–30]. On-chip sensors can also be mass-produced to relatively low-cost and reference sensors can be fitted on the same chip to reduce sensitivity to ambient conditions. In long term, a chip can be fitted with multiple sensor, sensitive to different measurands.

The main goal of this thesis is to investigate the effect that temperature, pressure and concentration of cryptophane-A, have on the sensitivity, selectivity and time-response of the sensors.

1.2 Interferometers

When two coherent light-waves overlap, interference occurs. This is because the complex amplitude U of the resulting wave is equal to the sum of the complex amplitudes of the superposed waves [31]:

$$U(\mathbf{r}) = U_1(\mathbf{r}) + U_2(\mathbf{r}) \tag{1.1}$$

with $\mathbf{r} = (x, y, z)$ being the wave coordinates. The optical intensity I of a monochromatic wave is the absolute square of its complex amplitude:

$$I(\mathbf{r}) = |U(\mathbf{r})|^2 \tag{1.2}$$

Interferometry, which interferometers are based upon, is a technique to use interference to extract information from superimposed waves. The idea is to combine two waves with the same frequency and create destructive and constructive interference based on the phase difference between the two waves. Interferometers are thus very sensitive to differences in path length and refractive index changes. The most commonly used source in interferometers are electromagnetic waves, usually light from a laser, but interference happens for everything propagating as waves. Acoustic interferometry and seismic interferometry is examples of interferometers based on other sources than light.

1.3 Mach-Zehnder interferometer

The Mach-Zehnder interferometer is one of the most commonly used interferometers. Figure 1.1 shows an outline for an on-chip MZI. The MZI splits a guided wave into two paths, one usually works as a reference arm, and the other as a sensing arm. After a certain distance, the sensing length, the light from the arms is combined, creating interference. The complex amplitudes for the two arms are given by:

$$U_{\mathrm{n}}(\mathbf{r}) = \sqrt{I_{\mathrm{n}}} \exp\left[-jkz\right] \exp\left[j\varphi_{\mathrm{n}}\right] \tag{1.3}$$

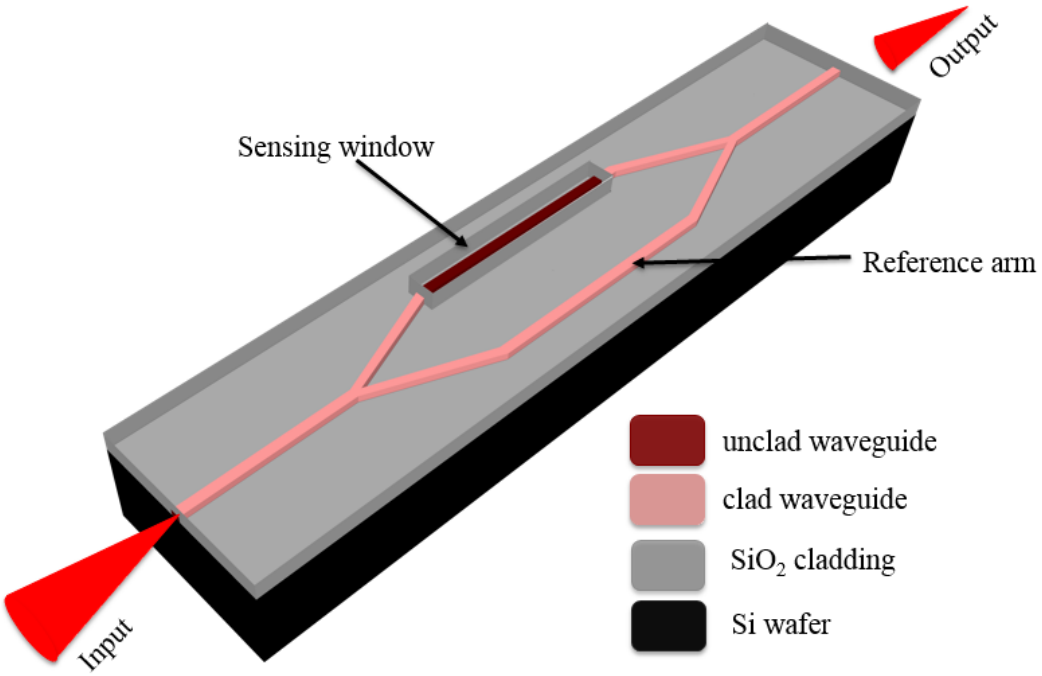

Figure 1.1: Outline of a waveguide Mach-Zehnder interferometer with one sensing window.

where k is the wavenumber and the waves propagate in the z-direction. Hence, using Equation 1.1 and Equation 1.2, the total optical intensity after combination of the two waves are:

$$I = I_1 + I_2 + 2\sqrt{I_1 I_2}\cos\Delta\varphi \tag{1.4}$$

where $\Delta\varphi = \varphi_2 - \varphi_1$.

1.4 Young interferometer

In this thesis, both Mach-Zehnder interferometer and Young interferometer have been used. Since both interferometers are consequently similar regarding their working principle, phase measured for one is valid for the other [14, 17, 21]. While the MZI has a single output, the Young interferometer arms are

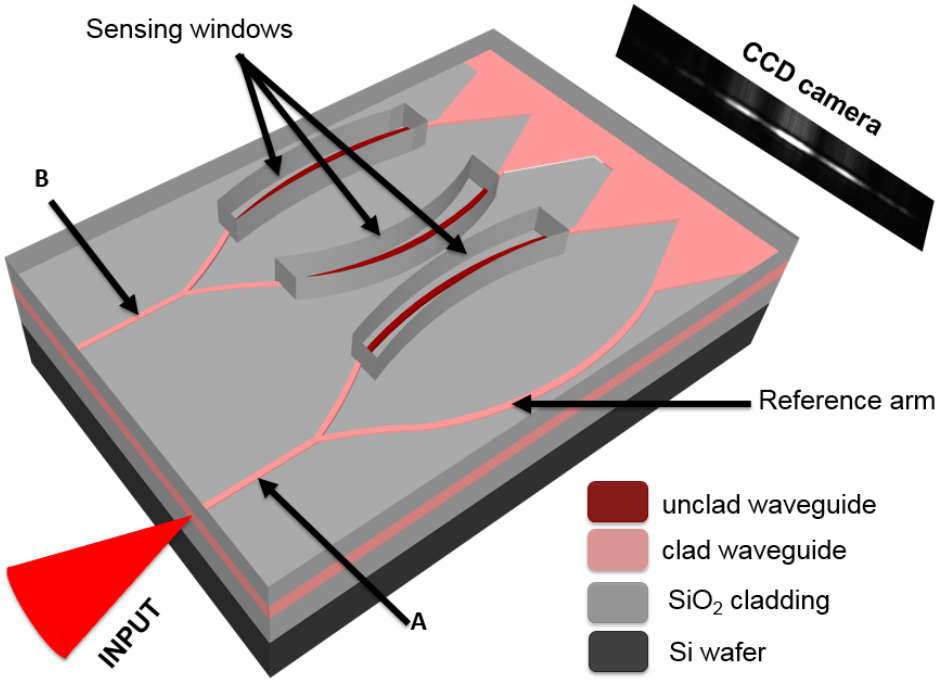

Figure 1.2: Outline of the waveguide Young interferometers with one (A) and two (B) sensing windows. The tapered areas are after the sensing windows giving fringes at the output. Figure from [17] Fig.1

not combined into a straight waveguide after the sensing length, but instead the arms go over to planar waveguides, as seen in Figure 1.2, a tapered area where the beams overlap in space and interfere. This results in a fringe pattern at the output facet of the chip. The phase can then be calculated from the position of the fringes and thus it is possible to separate a change in phase from a change in amplitude [32].

The beams overlap with an angle $\theta/2$ from the z-axis, where θ is the angle between the two arms at the facet. Looking at the interferometer propagating in the z-direction and the arms laying in the xz-plane, the waves coming from the arms can be described as:

$$\begin{aligned} U_1(\mathbf{r}) &= \sqrt{I_1(\mathbf{r})}\exp\left[-jk\left(z\cos\frac{\theta}{2} - x\sin\frac{\theta}{2}\right)\right]\exp\left[j\varphi_1\right] \\ U_2(\mathbf{r}) &= \sqrt{I_2(\mathbf{r})}\exp\left[-jk\left(z\cos\frac{\theta}{2} + x\sin\frac{\theta}{2}\right)\right]\exp\left[j\varphi_2\right] \end{aligned} \tag{1.5}$$

Using Equation 1.1 and Equation 1.2 the intensity I can be solved at $z = 0$, yielding:

$$I(\mathbf{r}) = I_1(\mathbf{r}) + I_2(\mathbf{r}) + 2\sqrt{I_1(\mathbf{r})I_2(\mathbf{r})}\cos\left(2k\sin\frac{\theta}{2}x + \Delta\varphi\right) \tag{1.6}$$

where $\Delta\varphi = \varphi_1 - \varphi_2$. Equation 1.6 can be expressed using the visibility:

$$V(\mathbf{r}) = \frac{I_{\max} - I_{\min}}{I_{\max} + I_{\min}} \tag{1.7}$$

$$= \frac{2\sqrt{I_1(\mathbf{r})I_2(\mathbf{r})}}{I_1(\mathbf{r}) + I_2(\mathbf{r})} \tag{1.8}$$

Thus, Equation 1.6 is written as:

$$I(\mathbf{r}) = 2\left(I_1(\mathbf{r}) + I_2(\mathbf{r})\right)\left[\frac{1 + V(\mathbf{r})\cos\left(2k\sin\frac{\theta}{2}x + \Delta\varphi\right)}{2}\right] \tag{1.9}$$

This calculation is done for infinite wide planar waves, while in the waveguide the beam is limited in the x- and y-direction. Since the tapered sections are equal, the field from the arms are the same in this section. Hence, Equation 1.9 can be written as:

$$I(x,y) = I_{\text{env}}(x,y)\left[\frac{1 + V(x,y)\cos\left(2k\sin\frac{\theta}{2}x + \Delta\varphi\right)}{2}\right] \tag{1.10}$$

where $I_{\text{env}}(x,y) = 2(I_1(x,y) + I_2(x,y))$. For the fundamental mode of the tapered section, this profile can be approximated by a Gaussian distribution, limiting the number of fringes in the lateral direction [14, 32]. In references [14, 32], a simplification of visibility $V = 1$ has been used. Then, with use of the trigonometric half-angle formula, Equation 1.10 can be simplified to:

$$I(x,y) = I_{\text{env}}(x,y)\cos^2\left(k\sin\frac{\theta}{2}x + \frac{\Delta\varphi}{2}\right) \tag{1.11}$$

To calculate the phase, both Equation 1.10 and Equation 1.11 will give the same answer by solving for the 3 first maximums. Using Equation 1.10:

$$2k \sin \frac{\theta}{2} x_1 + \Delta\varphi = -2\pi \tag{1.12}$$

$$2k \sin \frac{\theta}{2} x_2 + \Delta\varphi = 0 \tag{1.13}$$

$$2k \sin \frac{\theta}{2} x_3 + \Delta\varphi = 2\pi \tag{1.14}$$

where x_1, x_2 and x_3 are the peak positions. We can now subtract Equation 1.14 from Equation 1.12, and insert this in Equation 1.13. Solving for $\Delta\varphi$ yields:

$$\begin{aligned} \Delta\varphi &= \frac{4\pi x_2}{x_3 - x_1} \\ &= \frac{2\pi}{d} x \end{aligned} \tag{1.15}$$

where d is the distance between the fringes and x is the position of one of the fringes. Thus the phase can be calculated only from following the position of one peak and knowing the distance between the peaks. In Figure 1.3, top picture, an example of fringes on the CCD is shown, while the bottom picture shows the peaks when rows are added together (blue line). Any change in in-coupling or amplitude changes will change the intensity of the peak, but will not lead to a shift of the pattern. Hence, a phase change will not be measured. In the normal Mach-Zehnder configuration, a change in amplitude is impossible to separate from phase change.

For experiments using the Young interferometer, a LabVIEW program was available giving the phase using Equation 1.10. In Figure 1.3, bottom picture, LabVIEW has fitted a line (orange) to the original data (blue line).

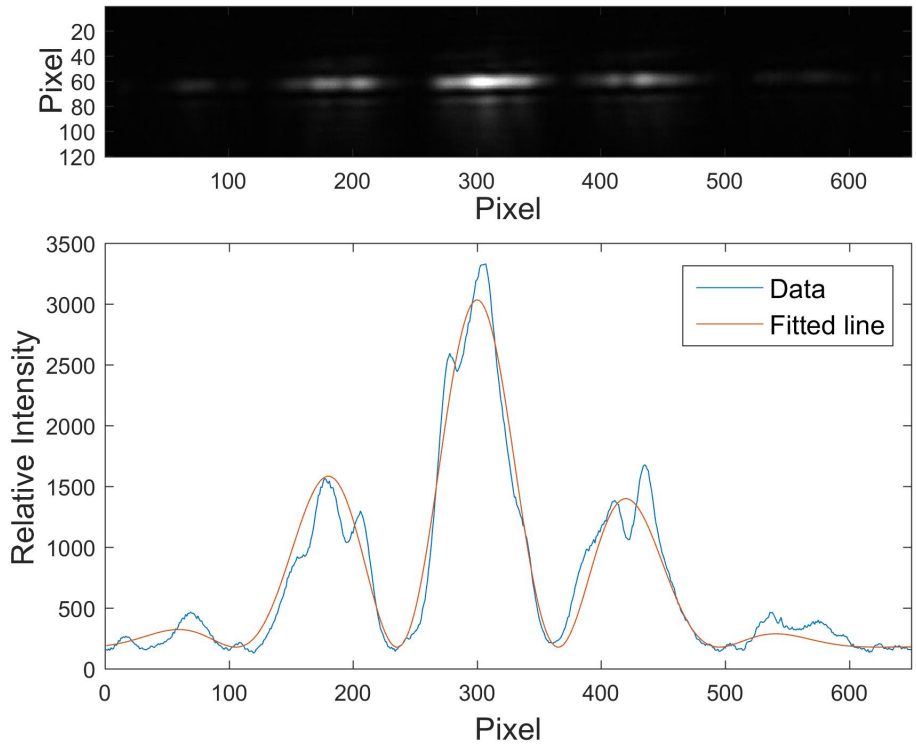

Figure 1.3: Showing the output fringes from a Young interferometer on the CCD (top) and after processing (bottom), blue line being the measured curve and the orange to fitted curve.

Chapter 2

Analytical analysis of sensitivity

In this chapter, the sensitivity of the interferometers are discussed. First, it is calculated how changes in refractive indexes and path length affect the phase measured by the interferometers. Then sensitivity of the different media are discussed for changes in pressure, temperature and methane concentration.

2.1 Phase sensitivity

When light travels through a waveguide, part of the field, the evanescent field, travels in the claddings, as seen in Figure 2.1. The distribution of the evanescent field depends on different factors, notably the waveguide geometry and the difference in refractive index between the core and the claddings. The waveguide Mach-Zehnder and Young interferometers use the principle of evanescent field sensing, by changing the refractive index of the media in one arm, the effective refractive index of this arm changes. Which again leads to a phase difference between the arms when combined, creating a change in the interference pattern.

The phase at the end of one arm can be described as:

$$\varphi = \frac{2\pi L}{\lambda_0} n_{\text{eff}} \tag{2.1}$$

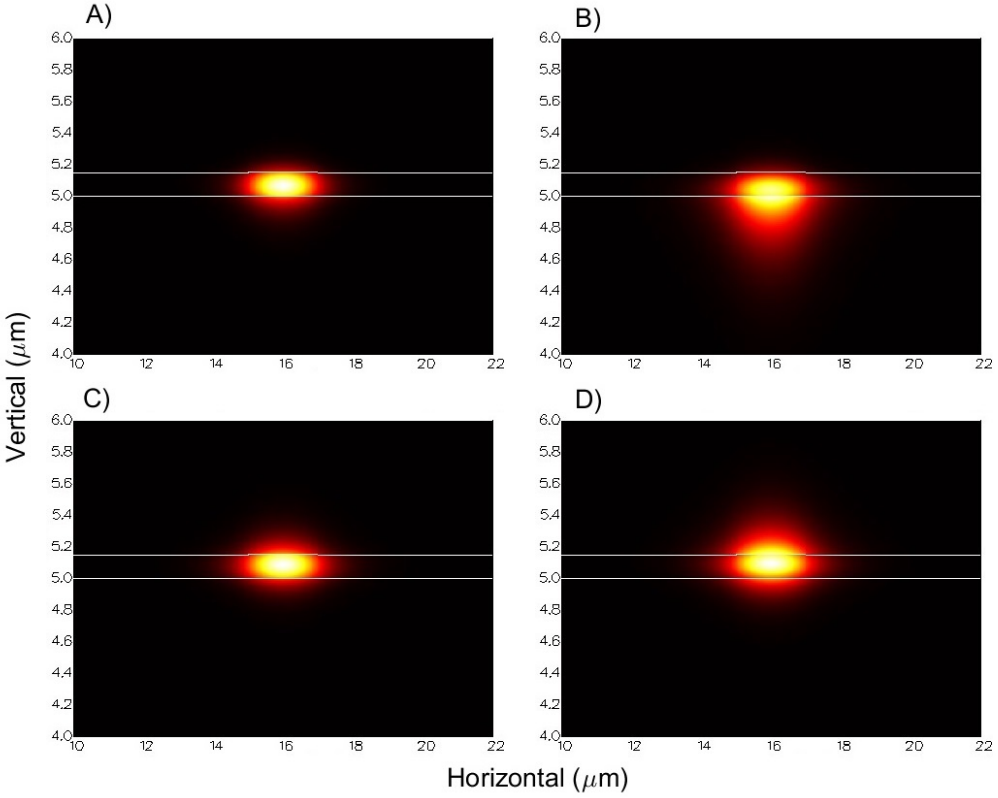

Figure 2.1: The intensity distribution in a rib waveguide when nitrogen clad for TE- (A) and TM- (B) mode, and SAN clad for TE- (C) and TM- (D) mode. Simulated with FimmWAVE.

where L is the sensing length, λ_0 is the wavelength in vacuum and n_{eff} is the change in the effective refractive index. The refractive index change might happen in the sensing layer only, or in more of the layers as well. To find a general solution, the refractive indexes are described as:

$$\underline{\mathbf{n}} = (n_{\text{tcl}}, n_{\text{core}}, n_{\text{bcl}}) \tag{2.2}$$

where n_{tcl}, n_{core} and n_{bcl} are the refractive indexes of the top cladding (sensing layer), core and bottom cladding respectively. The effective refractive index can be written as a function of refractive indexes for constant waveguide geometry and wavelength:

$$n_{\text{eff}} = F(\underline{\mathbf{n}}) \tag{2.3}$$

Using this, the phase change in one arm due changing a parameter A (e.g., temperature, pressure, methane concentration) can be formulated:

$$\begin{aligned}
\frac{\mathrm{d}\varphi}{\mathrm{d}A} &= \frac{2\pi L}{\lambda_0}\nabla F(\underline{\mathbf{n}}) \cdot \frac{\mathrm{d}\underline{\mathbf{n}}}{\mathrm{d}A} && (2.4)\\
&= \frac{2\pi L}{\lambda_0}\left(\frac{\partial F(\underline{\mathbf{n}})}{\partial n_{\mathrm{tcl}}}\frac{\mathrm{d}n_{\mathrm{tcl}}}{\mathrm{d}A} + \frac{\partial F(\underline{\mathbf{n}})}{\partial n_{\mathrm{core}}}\frac{\mathrm{d}n_{\mathrm{core}}}{\mathrm{d}A} + \frac{\partial F(\underline{\mathbf{n}})}{\partial n_{\mathrm{bcl}}}\frac{\mathrm{d}n_{\mathrm{bcl}}}{\mathrm{d}A}\right) && (2.5)\\
&= \frac{2\pi L}{\lambda_0}\left(S_{\mathrm{tcl}}\frac{\mathrm{d}n_{\mathrm{tcl}}}{\mathrm{d}A} + S_{\mathrm{core}}\frac{\mathrm{d}n_{\mathrm{core}}}{\mathrm{d}A} + S_{\mathrm{bcl}}\frac{\mathrm{d}n_{\mathrm{bcl}}}{\mathrm{d}A}\right) && (2.6)
\end{aligned}$$

where S_{tcl}, S_{core} and S_{bcl} are the homogeneous sensitivities defined as change of effective refractive index, to the rate of change of the refractive indexes of the different media. Equation 2.6 is only valid when the change A is uniform along one arm. For change of temperature or pressure this is true, at least after some stabilization time, changing all refractive indexes. For change in concentration of methane (x), since the gas does not diffuse through the core layer, $\mathrm{d}n_{\mathrm{core}}/\mathrm{d}x$ and $\mathrm{d}n_{\mathrm{bcl}}/\mathrm{d}x$ are equal to 0.

In an interferometer, two arms are used to find the phase, thus the total phase change is:

$$\frac{\mathrm{d}\varphi}{\mathrm{d}A} = \frac{\mathrm{d}\varphi_1}{\mathrm{d}A} - \frac{\mathrm{d}\varphi_2}{\mathrm{d}A} \tag{2.7}$$

with the indexes 1 and 2 referring to the different arms. Assuming the parameter A changes uniformly for both arms, the core and bottom cladding is the same for both arms. Hence, Equation 2.6 and Equation 2.7 can be solved as:

$$\begin{aligned}
\frac{\mathrm{d}\varphi}{\mathrm{d}A} =& \frac{2\pi L}{\lambda_0}\left[S_{\mathrm{tcl},1}\frac{\mathrm{d}n_{\mathrm{tcl},1}}{\mathrm{d}A} - S_{\mathrm{tcl},2}\frac{\mathrm{d}n_{\mathrm{tcl},2}}{\mathrm{d}A} + \left(S_{\mathrm{core},1} - S_{\mathrm{core},2}\right)\frac{\mathrm{d}n_{\mathrm{core}}}{\mathrm{d}A}\right.\\
&\left. + \left(S_{bcl,1} - S_{bcl,2}\right)\frac{\mathrm{d}n_{bcl}}{\mathrm{d}A}\right]
\end{aligned} \tag{2.8}$$

2.2 Pressure sensitivity

2.2.1 Gas

The Lorentz-Lorenz equation of a diluted gas is given as [33, 34]:

$$n^2 - 1 = \frac{3AP}{RT} \tag{2.9}$$

where A is the molar refractivity, proportional to the polarizability of the gas, P is pressure, R is the universal gas constant and T is absolute temperature. Assuming the ideal gas law, A can be assumed constant, giving:

$$n^2 - 1 = (n_0^2 - 1)\frac{T_0}{P_0}\frac{P}{T} \tag{2.10}$$

with n_0 being the refractive index at T_0 and P_0. Hence, for any diluted gas under the approximation of the ideal gas law, the refractive index dependency on pressure at a given temperature T_0 can be found as the derivative of Equation 2.10:

$$\frac{\mathrm{d}n}{\mathrm{d}P} = \frac{(n_0^2 - 1)\frac{T_0}{P_0}\frac{1}{T}}{2\sqrt{(n_0^2 - 1)\frac{T_0}{P_0}\frac{P}{T} + 1}} \tag{2.11}$$

$$= \frac{n^2 - 1}{2nP} \tag{2.12}$$

2.2.2 Silica and Silicon Nitride

The Gladstone-Dale relation approximates the density of a glass as directly proportional to its refractive index [35]:

$$n - 1 \propto \rho \tag{2.13}$$

This relationship is valid for many polymorphs of SiO_2, as shown by Maj et al. [36]. By assuming that all compression is happening in one axis, the change in thickness of the silica cladding due to pressure can be estimated

Table 2.1: Refractive index dependence on pressure of silica and silicon nitride as calculated from Equation 2.16

Substance	n	E (kbar)	$\mathrm{d}n/\mathrm{d}P$ (10^{-6}/bar)
SiO_2	1.45	731 [38]	0.63
Si_3N_4	2.01	1660 - 2970 [39]	0.34 - 0.60

with Young's modulus:

$$\Delta h = -h_0 \frac{P - P_0}{E} \tag{2.14}$$

where Δh and h_0 is the change in thickness and the thickness at atmospheric pressure respectively, P is pressure, P_0 is atmospheric pressure (1 bar) and E is the Young's modulus. By using $\rho = m/V$ and $V = A_0(h_0 + \Delta h)$ Equation 2.13 is rewritten as:

$$n - 1 = (n_0 - 1)\frac{E}{E - (P - P_0)} \tag{2.15}$$

with n_0 being refractive index at 1 bar. The refractive index change with pressure ($\mathrm{d}n/\mathrm{d}P$) can be calculated from the derivative of Equation 2.15:

$$\frac{\mathrm{d}n}{\mathrm{d}P} = (n_0 - 1)\frac{E}{(E - (P - P_0))^2} \tag{2.16}$$

$$\approx \frac{(n_0 - 1)}{E} \tag{2.17}$$

where Equation 2.17 is a simplification assuming $E >> (P - P_0)$.

To my knowledge, a direct relationship between refractive index and pressure has not been reported for silicon nitride. Different hard materials, especially materials containing Silicon, have shown a linear dependency of refractive index with density [36, 37]. Supposing that Equation 2.13 is a good approximation for Si_3N_4, then the refractive index dependence on pressure is inversely proportional to Young's modulus, as described in Equation 2.17. $\mathrm{d}n/\mathrm{d}P$ can thus be calculated for silica and silicon nitride at 25°C. Results are given in Table 2.1.

2.2.3 Gas solubility in SAN

When increasing pressure in the gas above the chip, the amount of gas dissolved in SAN increases, hence compensating for the partial pressure on the outside with internal pressure from gas molecules. When pressure is increased it might be counter-acted by compression of the material, increase of dissolved gas or a combination. Solubility S is defined as the concentration a solute can be dissolved in a material at certain pressures. The equilibrium concentration C is then defined as:

$$C = SP \tag{2.18}$$

with S being solubility and P the applied pressure. Solubility is approximated to be constant for methane and nitrogen for the small pressure changes applied in this thesis. It is also assumed that nitrogen and methane do not penetrate silica and silicon nitride.

Refractive index of a material can empirically be described as:

$$n - 1 = \sum_s N_\mathrm{s} M_\mathrm{s} \tag{2.19}$$

with N_s being the number of a certain molecule inside a certain volume and M_s the contribution this molecule bring the refractive index respectively. Hence for when nitrogen gas solves in SAN the refractive index can be written as:

$$\begin{aligned} n - 1 &= N_\mathrm{SAN} M_\mathrm{SAN} + N_{\mathrm{N}_2} M_{\mathrm{N}_2} \\ &= (n_\mathrm{SAN} - 1) + N_{\mathrm{N}_2} M_{\mathrm{N}_2} \end{aligned} \tag{2.20}$$

A relation N_SAN and N_{N_2} can be written in terms of the concentration C:

$$N_{\mathrm{N}_2} \propto N_\mathrm{SAN} SP \tag{2.21}$$

using a proportionality constant k, Equation 2.20 can be written as:

$$n - 1 = (n_\mathrm{SAN} - 1) + k N_\mathrm{SAN} M_{\mathrm{N}_2} SP \tag{2.22}$$

This equation can be solved by setting $S = 1$ and $P = 1$ atm, in that scenario the refractive index would be:

$$(n-1)_{P=1\text{ atm}} = (n_{\text{SAN}}-1)_{P=1\text{ atm}} + (n_{\text{N}_2}-1)_{P=1\text{ atm}} \tag{2.23}$$

Hence, $kN_{\text{SAN}}M_{\text{N}_2} = (n_{\text{N}_2}-1)_{P=1\text{ atm}} = 2.68 \cdot 10^{-4}$. Then Equation 2.22 becomes:

$$n - 1 = (n_{\text{SAN}} - 1) + 2.68 \cdot 10^{-4} SP \tag{2.24}$$

And the pressure dependency can be calculated from the derivative:

$$\frac{\mathrm{d}n}{\mathrm{d}P} = \frac{\mathrm{d}n_{\text{SAN}}}{\mathrm{d}P} + 2.68 \cdot 10^{-4} S \tag{2.25}$$

2.3 Temperature sensitivity

In this section, the refractive index sensitivities to temperature are discussed for the different cladding materials. Temperature sensitivities are given for 1070 nm wavelength, because this wavelength was used for temperature measurement (see more in section 5.1).

For air, the refractive index can be approximated by Equation 2.10, hence, the temperature sensitivity can by found from the derivative:

$$\frac{\mathrm{d}n}{\mathrm{d}T} = \frac{(n_0^2-1)\frac{T_0}{P_0}\frac{P}{T^2}}{2\sqrt{(n_0^2-1)\frac{T_0}{P_0}\frac{P}{T}+1}} \tag{2.26}$$

$$= -\frac{n^2-1}{2nT} \tag{2.27}$$

In Figure 2.2, the temperature sensitivity of air is plotted against temperature. As seen, the rate of change is decreasing with temperature. For 25°C, the sensitivity is -0.89·10^{-6}RIU/°C. The temperature sensitivities of other the cladding materials, SAN, silica, silicon nitride and oil, were taken from literature as summarized in Table 2.2.

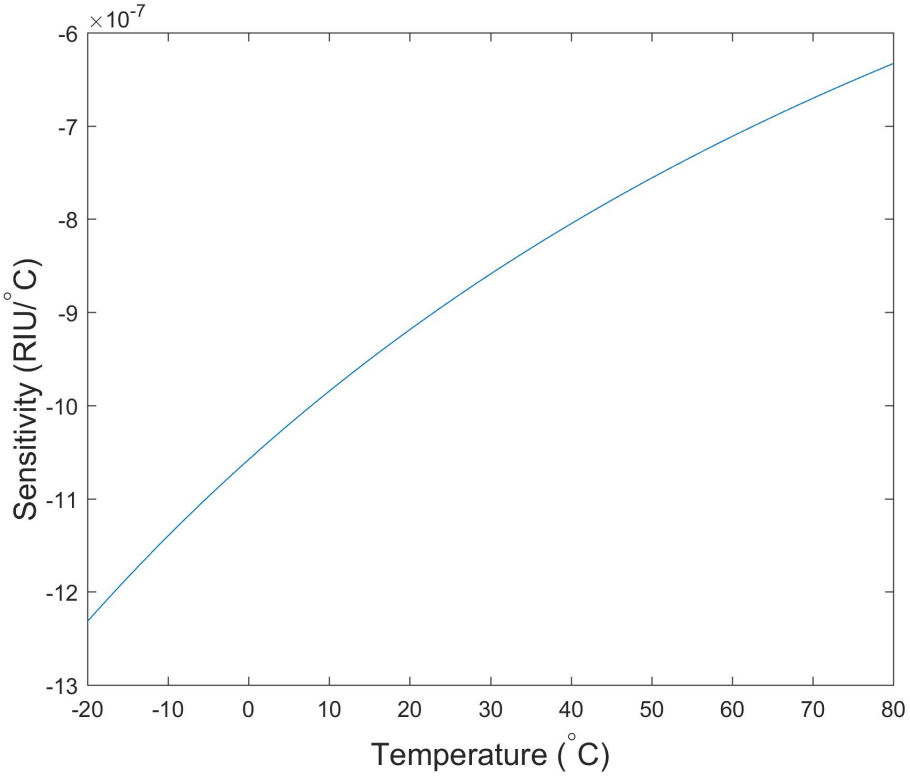

Figure 2.2: Temperature sensitivity, dn/dT, of air between -20°C and 80°C.

Table 2.2: Temperature sensitivities, dn/dT, for different materials at 25°C and 1070 nm wavelength.

Medium	n	dn/dT (10^{-6}/°C)	Ref.
Air	1.00	-0.89	-
Silica	1.45	12.9	[40]
Oil	1.47	-371	Spec.
SAN	1.56	-110	[41]
Silicon Nitride	2.01	24.5	[42]

2.4 Methane sensitivity

2.4.1 SAN

In the case where there is methane in the nitrogen at a concentration x, the refractive index of SAN with the dissolved gas can be written like Equation 2.22:

$$n - 1 = (n_{\text{SAN}} - 1) + k_1 N_{\text{SAN}} M_{\text{N}_2} S_{\text{N}_2,\text{SAN}} P(1-x) + k_2 N_{\text{SAN}} M_{\text{CH}_4} S_{\text{CH}_4,\text{SAN}} Px \tag{2.28}$$

with $S_{\text{N}_2,\text{SAN}}$ and $S_{\text{CH}_4,\text{SAN}}$ being the solubility of nitrogen and methane in SAN respectively. If $x = 0$, then pure nitrogen is flowing, as already shown in subsection 2.2.3. Thus, $k_1 N_{\text{SAN}} M_{\text{N}_2} = (n_{\text{N}_2} - 1)_{P=1\text{ atm}} = 2.68 \times 10^{-4}$. On the other hand, if $x = 0$, then pure methane is flowing. This can be solved in the same way as pure nitrogen, giving $k_2 N_{\text{SAN}} M_{\text{CH}_4} = (n_{\text{CH}_4} - 1)_{P=1\text{ atm}} = 4.37 \times 10^{-4}$. Hence, Equation 2.28 can be solved as:

$$n - 1 = (n_{\text{SAN}} - 1) + 2.68 \times 10^{-4} S_{\text{N}_2,\text{SAN}} P(1-x) + 4.37 \times 10^{-4} S_{\text{CH}_4,\text{SAN}} Px \tag{2.29}$$

Thus, the dependency of refractive index on concentration can be calculated from the derivative:

$$\frac{\mathrm{d}n}{\mathrm{d}x} = (4.37 \times 10^{-4} S_{\text{CH}_4,\text{SAN}} - 2.68 \times 10^{-4} S_{\text{N}_2,\text{SAN}})P \tag{2.30}$$

2.4.2 SAN doped with cryptophane-A

Cryptophanes are synthetic organic compounds with a cage-like structure. The cavity volume is decided by properties of the cryptophane. Cryptophane-A, the smallest in the series, has shown to have given an internal cavity suitable for trapping methane [26–28]. Some other molecules, chlorofluorocarbons, radon and xenon, might also be trapped by cryptophane-A. This effect has to be further investigated, but is outside of the scope of this thesis. Experimentally, nitrogen and methane are used from calibrated gas bottles, hence there is no chlorofluorocarbons, radon or xenon

contaminating the experiments. Cryptophane-A is thus used to reversibly trap a higher amount of methane in the SAN-layer than what naturally would be dissolved, but proportional to the outside concentration. Thus, increasing the sensitivity of the sensor drastically. The use of cryptophane-A is the key step to the highly sensitive, selective sensing layer.

The refractive index of SAN doped with cryptophane-A can be written from Equation 2.19 as:

$$n - 1 = N_{\mathrm{Pol}} M_{\mathrm{Pol}} + N_{\mathrm{N_2}} M_{\mathrm{N_2}} + N_{\mathrm{CH_4}} M_{\mathrm{CH_4}} + N_{\mathrm{Trapped}} M_{\mathrm{CH_4}} \tag{2.31}$$

with the index Pol being the polymer made up by SAN and cryptophane-A, without trapped molecules, and the index Trapped being the number of trapped methane molecules by the cryptophane. Here it is distinguished between the methane that would dissolve in the polymer naturally and the methane trapped by cryptophane-A. In the same way as in subsection 2.4.1 this can be rewritten using the solubilities, pressure and refractive indexes:

$$\begin{aligned} n - 1 = (n_{\mathrm{Pol}} - 1) &+ 2.68 \times 10^{-4} S_{\mathrm{N_2,Pol}} P(1 - x) \\ &+ 4.37 \times 10^{-4} S_{\mathrm{CH_4,Pol}} P x + F\left(x, c, P\right) \end{aligned} \tag{2.32}$$

where n_{Pol} is the refractive index of the polymer without trapped molecules, $S_{\mathrm{N_2,Pol}}$ and $S_{\mathrm{CH_4,Pol}}$ being the solubilities of nitrogen and methane in the polymer, P the pressure in the outside gas, x the concentration of methane in nitrogen, c the concentration of cryptophane-A to SAN, and F being for the refractive index contribution of trapped methane molecules in the polymer. $S_{\mathrm{CH_4,Pol}}$ is thus not including the increased amount of methane due to trapping. Hence, the sensitivity of refractive index to concentration of methane in nitrogen can be found by the derivative:

$$\frac{\mathrm{d}n}{\mathrm{d}x} = 4.37 \times 10^{-4} S_{\mathrm{CH_4,Pol}} P - 2.68 \times 10^{-4} S_{\mathrm{N_2,Pol}} P + \frac{\partial F\left(x, c, P\right)}{\partial x} \tag{2.33}$$

Chapter 3

Experimental setup

In this chapter, the experimental setup will be described. The setup itself is divided into three parts; optical components, chip holder and gas flow system. Further on, the design, the fabrication and the preparation of the chip is described. A detailed list with manufacturers and product information for all parts is included in Appendix A.

3.1 Optical components

In Figure 3.1, a schematic of the optical setup is shown; all components are fixed to the optical table to reduce vibrations. The collimated output beam from the laser passes through a half-wave plate to adjust the polarization direction of the linearly polarized laser beam. The beam then passes through two lenses (Figure 3.1, lens 1 and 2) at distance $d = f_1 + f_2$ to expand the beam to match the input objective. Between the beam-expander and the input objective a polarizer is placed; this is used to select between the transverse electric (TE) or the transverse magnetic (TM) polarization. A 25x microscope objective (Figure 3.1, lens 3) focuses the beam on the chip. The objective is placed on a 3-axis Piezo controller to be able to accurately position the objective so that the laser light is focused on the chip facet and the best coupling (into the waveguide) is achieved. After the beam passes through the chip, a 10x microscope objective (Figure 3.1, lens 4) focuses

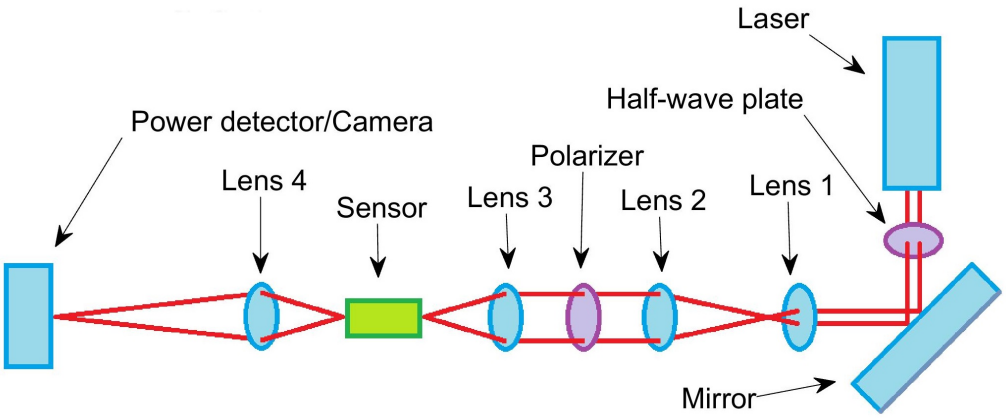

Figure 3.1: Optical components of the setup.

the output power to either a power detector or a CCD camera. The power detector has an iris mounted in front of it that can be adjusted to filter out spurious light from the neighboring planar waveguides. Absorptive neutral density filters were used to reduce the power to match the set range of the preamplifier of the power detector. The filters were placed both between the output objective and the detector, and between the polarizer and the input objective. Reducing the power before the chip also help to reduce temperature effects coming from the high power of the laser.

A microscope with a camera is mounted on a 2-D translation stage to image the top surface of the chip. This is used to help couple the laser into the waveguides, and observe how light propagates along the guiding structures. Measurement of light scattering from the chip surface was also used to estimate propagation loss as described in section 4.2.

3.2 Chip holder

An aluminum block on a 1-D translation stage makes the basis for the chip holder. A slot for a Peltier-element is drilled out and a custom made aluminum plate working as a chip holder is placed on top. Thermal paste is used between the Peltier-element and the aluminums pieces to enhance thermal conductivity and a thermistor, providing feedback to a temperature

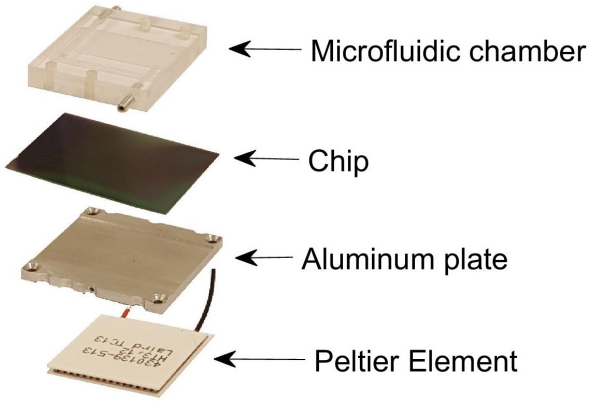

Figure 3.2: Overview of the components in the chip holder.

controller, is placed in the top aluminum plate. The chip is then positioned on top of the assembly and covered from the top by a micro fluidic chamber that can be screwed into the top aluminum block. The assembly of the chip holder is seen in Figure 3.2, except the aluminum block. The temperature of the sample holder and thus the chip is controlled by a temperature controller to a precision of 1 mK; this precision is needed to compensate for the high temperature sensitivity of the sensor as shown in section 5.1.

3.3 Gas flow system

The layout of the gas flow system is shown in Figure 3.3. Two mass flow controllers (MFC) in a T-junctions were used to regulate the flow through the system, where one was connected to nitrogen and the other to methane. Calibrated gas cylinders were used with 2 mol% or 4.4 mol% methane in nitrogen (AGA, ±2.00% relative uncertainty). The MFCs were controlled by a LabVIEW program that kept the total flow through the microfluidic chamber constant, while varying the concentration by changing the relative flows with the two respective MFCs. Before reaching the chip surface, the gas passes through a small 5 ml mixing chamber to better mix the gases and

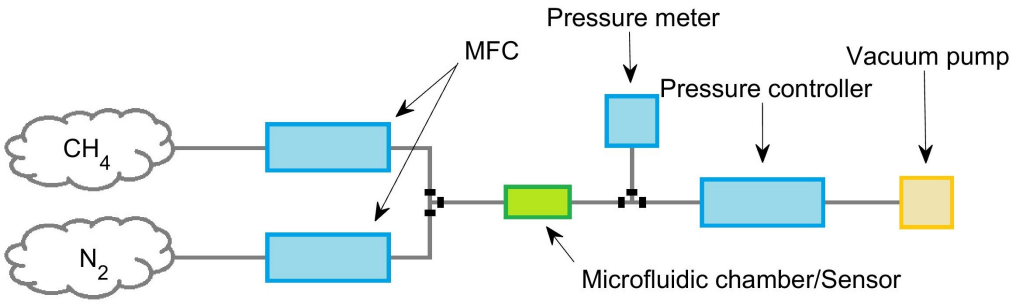

Figure 3.3: The setup of the gas flow system.

homogenize the gas temperature. After the microfluidic chamber, another T-junction splits the gas to a pressure meter and a pressure controller. After the pressure controller, the gas was either released into the room, or was lead further to a vacuum pump if pressures under 1 atm were needed. The concentration of methane was monitored with a commercial Franatech TDLS Methane sensor after the pressure controller.

3.4 Chip design

The chip design was chosen when I joined this project, and the chips were already fabricated. This section will explain the background for choosing the design of the chip, but the work is done mainly by Firehun Tsige Dullo, Susan Lindecrantz and Olav Gaute Hellesø.

On-chip interferometers were used partially due to there small size. On the chip of dimensions 25×40×1 mm, a total of 36 Mach-Zehnder interferometers and 24 Young interferometers, with different rib widths and sensing lengths, are available. Plus a number of straight waveguides, Y-junctions and more. This shows how small an on-chip sensor can be made. It is also possible to, in the future, add reference sensors or have sensors sensing different media on the same chip.

Rib waveguides were chosen because of lower propagation loss than a strip

waveguide [43], but only 4-8% less sensitive [44]. Rib waveguides also give good possibilities to control which mode light propagates in, dependent on core thickness, rib height and rib width [44, 45]. After careful simulations, the waveguides were designed with 150 nm core thickness, 5 nm rib height and rib widths of 1.5 µm, 2 µm and 3 µm. These dimensions gave single-mode options for both TE and TM polarization, and wavelengths of 785 nm and 1070 nm (section 5.1) [46]. In Figure 3.4, a cross-section of a rib waveguide is shown with, silica working as reference arm (1) and air clad sensing window (2).

Mach-Zehnder interferometers were designed as shown in Figure 1.1. A symmetric Y-junction consisting of two S-bends with radius 4 mm splits the two arms to a center-to-center distance of 100 µm. Either one or both of the arms has a sensing window of 3 cm, 2 cm or 1 cm length. Another Y-junction of same design combines the arms into a straight waveguide. If only one arm has a sensing window (1SW), we speak of an asymmetric or unbalanced

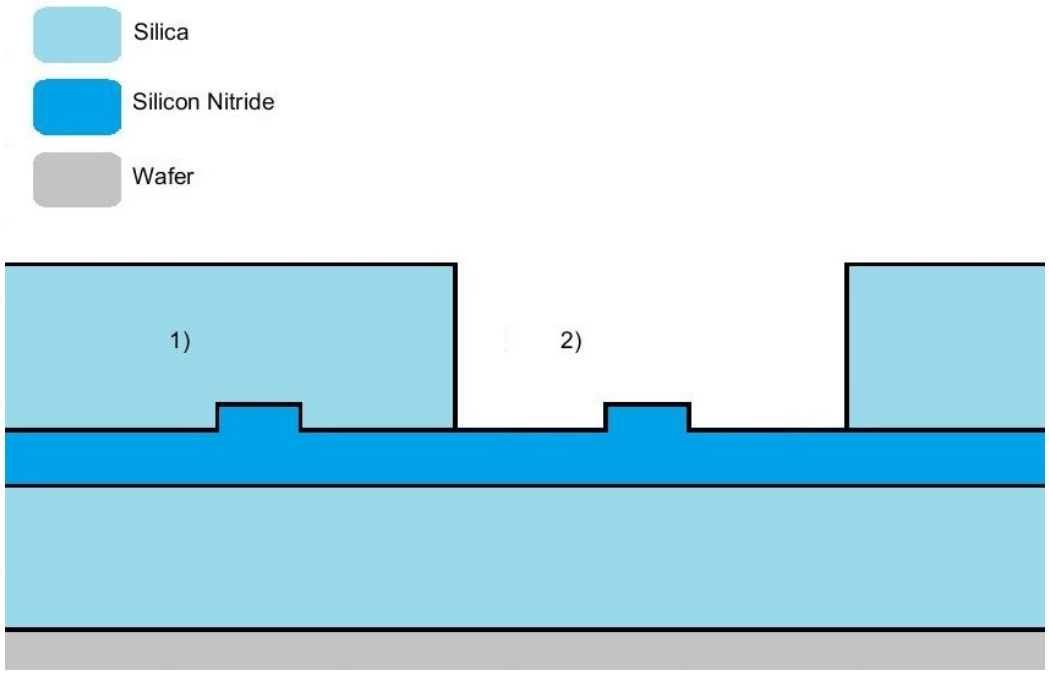

Figure 3.4: Cross-section of rib waveguides with silica (1) on reference arm and (2) a sensing window. Dimensions are not to scale.

interferometer with silica on the reference arm. With sensing windows on two arms (2SW), a symmetric or balanced interferometer is achieved.

Young interferometers were designed as shown in Figure 1.2. A symmetric Y-junction splits a waveguide in two waveguide arms with average separation of 395 µm. Sensing windows were made on one or both of the arms, all 2 cm long. Towards the end the of the chip the waveguides are expanded, giving two inclined, tapered sections.

3.5 Chip fabrication

The waveguides were fabricated by IMB-CNM, CSIC, in Barcelona, Spain, according to Prieto et al.[45]. A 1 µm thick silica (SiO_2) layer of refractive index 1.45 was grown by thermal oxidation of a silicon wafer. A 150 nm core layer of silicon nitride (Si_3N_4) with refractive index 2.01 is deposited by low-pressure chemical vapor deposition (LPCVD) at 800°C. A 5 nm height rib structure was etched by reactive ion etching (RIE). Finally, a 1 µm silica protective layer was deposited by plasma enhanced chemical vapor deposition (PECVD) at 300 °C. The sensing arms were opened in the protective layer by RIE and wet etching, giving sensing windows 1 µm deep, 50 µm wide and 1, 2 and 3 cm long [14, 44, 45].

3.6 Chip preparation

Cleaning procedures were followed to keep the chips quality. A simple cleaning procedure was done when a chip had been out of use for a while and collecting dust. The chip was then cleaned with a clean-room swab soaked in acetone before it was sonicated successively in acetone, isopropanol and distilled water for 5 minutes in each solvent before it was dried of using by N_2 gas. The chip was then introduced to a solution of 5% Hellmanex in distilled water for 10 minutes at 70°C, and afterwards rinsed in distilled water and dried using N_2 gas.

If the chip previously had been used with either oil or polymer on top,

the chip needed to be completely recycled. The first step is then to put the chip in Dynasolve for at least 30 min, preferably overnight. The chip was then cleaned as described above before it was sonicated in a 1:1 solution of methanol and hydrochloric acid (HCl, 37%) for 10 minutes. After being rinsed in distilled water and dried using N_2 gas, the chip was introduced to air plasma 10 minutes, rinsed with isopropanol, distilled water and then dried using N_2 gas.

The cleaned or recycled chip went through a silanization procedure before a new polymer layer was to be deposited on the chip, to increase the adhesion of the polymer to the glass. A recycled chip was first put in UV light for 1.5 hour to activate the surface, before immersion in a 1% (3-Aminopropyl)triethoxysilane (APTES) to ethanol solution for 1 hour. The chip was then sonicated in ethanol for 2 minutes before rinsing it in ethanol, distilled water and dried using N_2 gas. Finally the chip was cured at 110°C for 1 hour.

To prepare a cryptophane-A doped polymer solution, the desired amount of cryptophane-A was first measured and added to a vial, then 900 μL of 1,1,2,2-Tetrachloroethane were added. This solution was mixed for 15 minutes before 3 pellets ($\approx$45 mg) Poly(Styrene-co-acrylonitrile), SAN, were added and mixed for further 1 hour. Directly after the chip was done curing from the silanization process, the solution was spin-coated on the chip for 2 minutes at 3000 rpm (Laurell WS-650MZ-23NPP/LITE) before it was cured overnight at 90°C. This gave a nice, homogeneous layer of SAN with measured thickness (KLA Tencor P-6) about 300-400 nm from the the surface and filling the sensing windows.

Chapter 4

System characterization

In this chapter, the noise originating in the system and the propagation loss in the waveguide is experimentally characterized. These are important factors to know the signal-to-noise ratio, limit-of detection and visibility of the sensors.

4.1 Noise measurements

The noise of a system is an important characteristics, that limits the system performance. The signal-to-noise ratio (SNR) is an important factor to determine the limit of detection (LOD) of the sensor. To evaluate both the short-term noise and long-term stability of the setup, the Allan deviation method was used. The Allan deviation (σ) compares the deviation of the output against integration time. By definition, random noise (white noise) can be averaged away. The longer you average, the smaller the noise gets ($\sigma \propto 1/\sqrt{t}$). Thus in an Allan plot, using logarithmic scales, white noise is represented by a straight, decreasing line. For other effects, like drift, the Allan deviation will increase when averaging over a longer period. Therefore, the Allan plot gives information of response time and system noise. A more detailed description of Allan deviation method (Allan variance) can by found in Werle et al. [47].

In Figure 4.1, the Allan deviations of the laser and detector are compared.

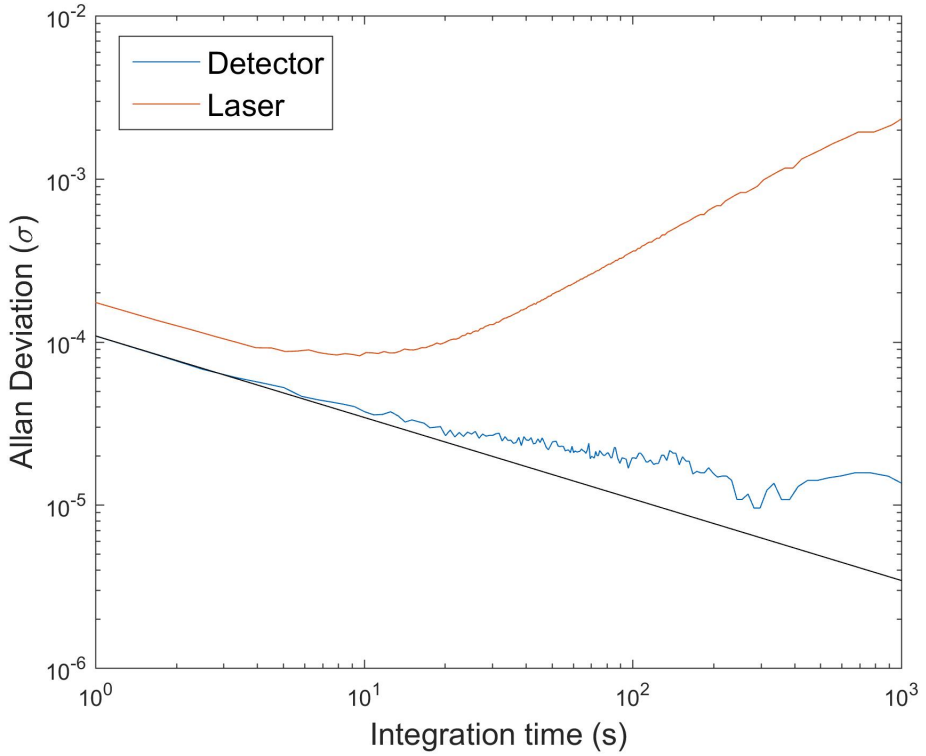

Figure 4.1: Allan deviation comparison between the amplifier (blue) and the laser (red). Theoretical white noise shown in black.

In both cases, the measurement setup consist of the laser pointed through a pinhole and onto the detector. When the detector noise is measured, the laser is simply switched off, so that both the electronic and the background noise were accounted for. As seen, the detector noise decreases with integration time, which means that it is dominated by white noise. But for integration times longer than around 20 seconds, the noise seems not to be only random. One explanation might be the dynamic range of the data acquisition (DAQ). The laser, on the other hand, starts drifting after 4 seconds. This drift is believed to be mostly mechanical, but some of it might be from the laser's characteristics. At this point the laser was placed on a 2D-translation stage, while later it was fixed to the optical table. This improvement should remove most of the mechanical noise, but there will still be some mechanical noise present that originates from thermal movement in stages. When the

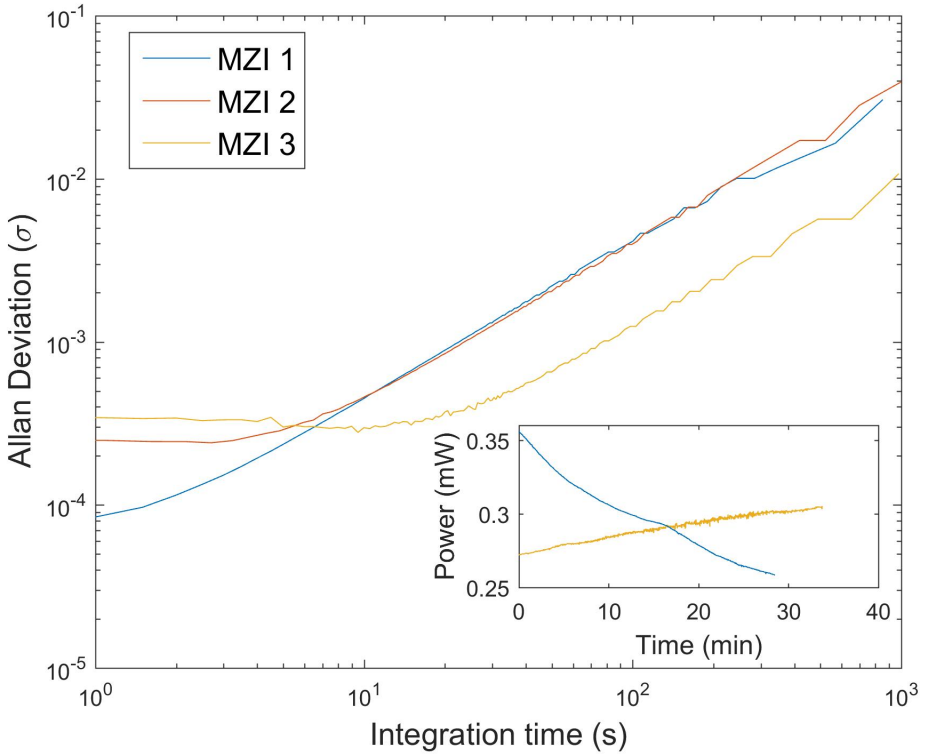

Figure 4.2: Allan deviation comparison of three Mach-Zehnder interferometers. The inset shows the power measured for two of the interferometers.

room temperature changes, it causes thermal expansion or contraction of the different stages. The Fabry-Pérot resonance might also be observed, especially when a beam expander, filters, half-wave plate and polarizer are involved.

To measure noise of the system, including the chip, three consecutive measurements on a asymmetric, 3 cm sensing length, Mach-Zehnder Interferometer was done with SAN as sensing layer. This result is shown in Figure 4.2. The noise within the first 3 seconds is a good representation of what the noise without drift would be, representing the standard deviation. It was experienced that after letting the system run for a long time, the system seemed to stabilize, thereby reducing the drift. The best result was found to be after 4 pm, when most people had left the building and after

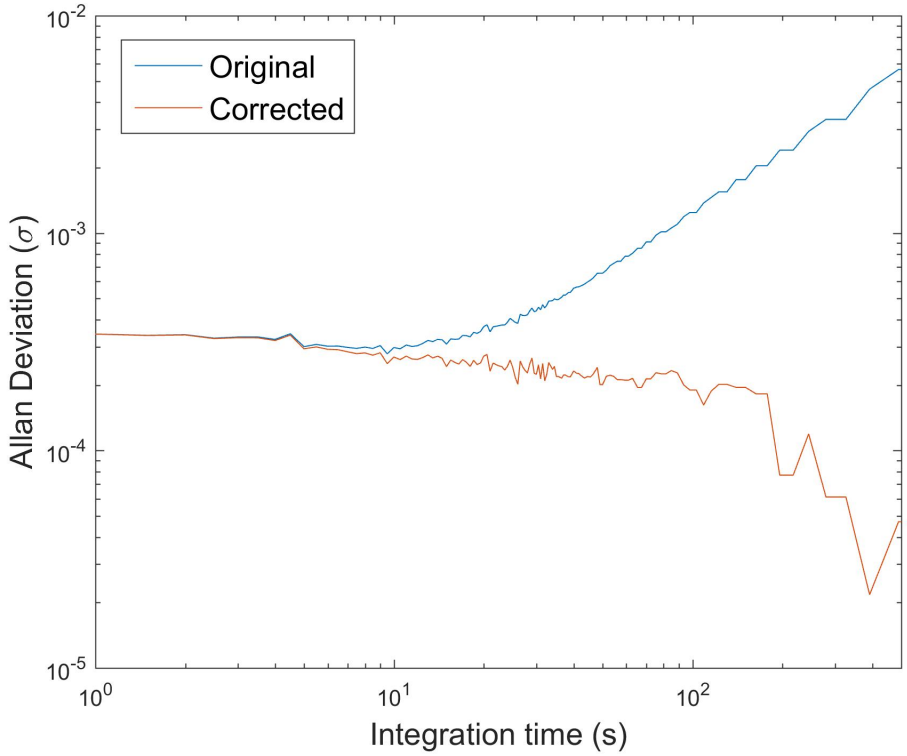

Figure 4.3: Allan deviation for MZI 3 in Figure 4.2 before and after correcting for linear drift.

stabilizing since the morning. As seen in Figure 4.2 for $t = 1$, MZI 1 was better stabilized when the measurement started than MZI 2 and MZI 3. On the other hand, MZI 3 has stabilized for the longest time, hence the drift is less than for MZI 1 and MZI 2. In the inset of Figure 4.2 the corresponding power measured from MZI 1 and MZI 3 is shown. MZI 3 was drifting less but was initially not stable. Hence, as the Allan plot shows, MZI 3 begins at a higher deviation, but it takes more time before the drift takes place.

Looking at the drift of the power for MZI 3, it can be approximated by a linear fit, and used to remove the drift. In Figure 4.3, the linear drift is removed from MZI 3, showing the Allan deviation after the correction. The corrected result does not have an upwards rise when drift takes over the noise. Linear drift often occurred during measurements. This might be for many reasons, but we expect that when turning on all systems, it takes time to

stabilize the instruments, especially the piezo and the room temperature. So leaving the system on for a while and recouple the laser into the waveguide, stabilizes the system and is an effective way to minimize the drift.

4.2 Propagation loss

The propagation loss was experimentally measured. The propagation loss gives information of how much light is lost in the waveguides, and thus how much light is needed to reach a certain output intensity. It is also used to measure the loss in the different arms, which is directly connected to the visibility.

Propagation loss of waveguides with width 2 µm was measured by taking

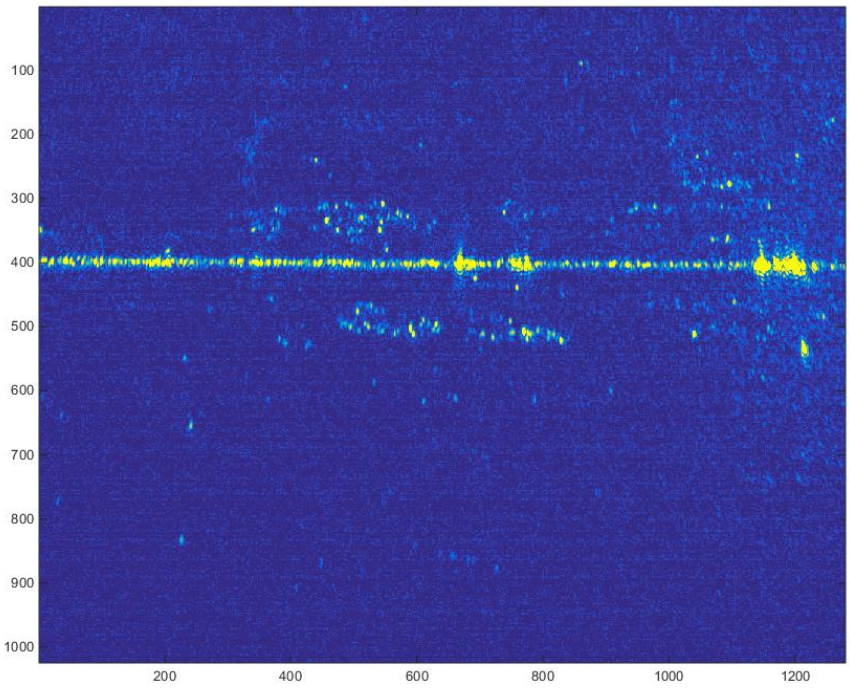

Figure 4.4: Image of the waveguide after the image has been processed from RGB to intensity scale and normalized.

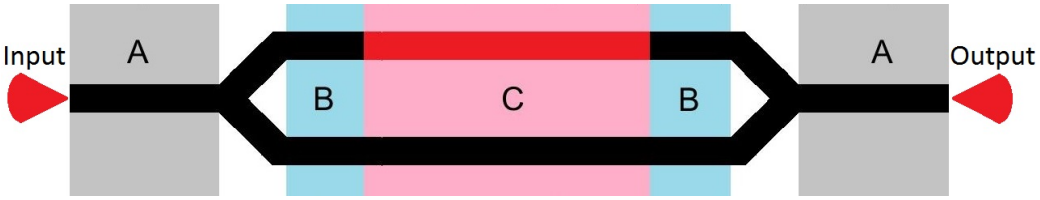

Figure 4.5: Overlay of a a MZI with A, B and C marking the different sections used for propagation loss measurement.

images of light scattered from the waveguide surface of an asymmetric Mach-Zehnder interferometer with 3 cm sensing length. The images are taken with camera on the microscope through a 4x microscope lens, see section 3.1 for more information. This method has shown to be suitable to measure relatively high propagation losses [43, 48]. The data is also used to estimate the loss due to scattering at the beginning and the ending of the sensing window and the quality of the Y-junction.

A layer of SAN was spin-coated on top of the chip following the procedure in section 3.6. Images are taken at different positions along the waveguide (Figure 4.5). The exposure time was chosen such that the brightest picture (closest to the input) was not saturated and then kept constant for all images. All images are converted to grayscale (only information about intensity) and corrected for using the flat field and the dark frame to remove the effects of pixel-to-pixel sensitivity variations and effect of dust or scratches on the CCD [49]. In Figure 4.4, an example of a processed image in gray-scale (intensity-scale) after flat-fielding is shown. The image is now represented by integer values between 0 and 255(8bit), representing the intensity of the pixels.

The images are processed such that only rows around the waveguide center are kept, and by removing locally saturated rows. Rows are then summed and a mean is taken to get a representation of relative intensity. Figure 4.6 shows the data points and a fitted curve for the sensing arm and the reference arm, respectively. All points are taken within the sensing window (Figure 4.5, area C). Since the arms have different cover media, they scatter differently, thus the scattering from the arms can not be compared directly, but the losses can

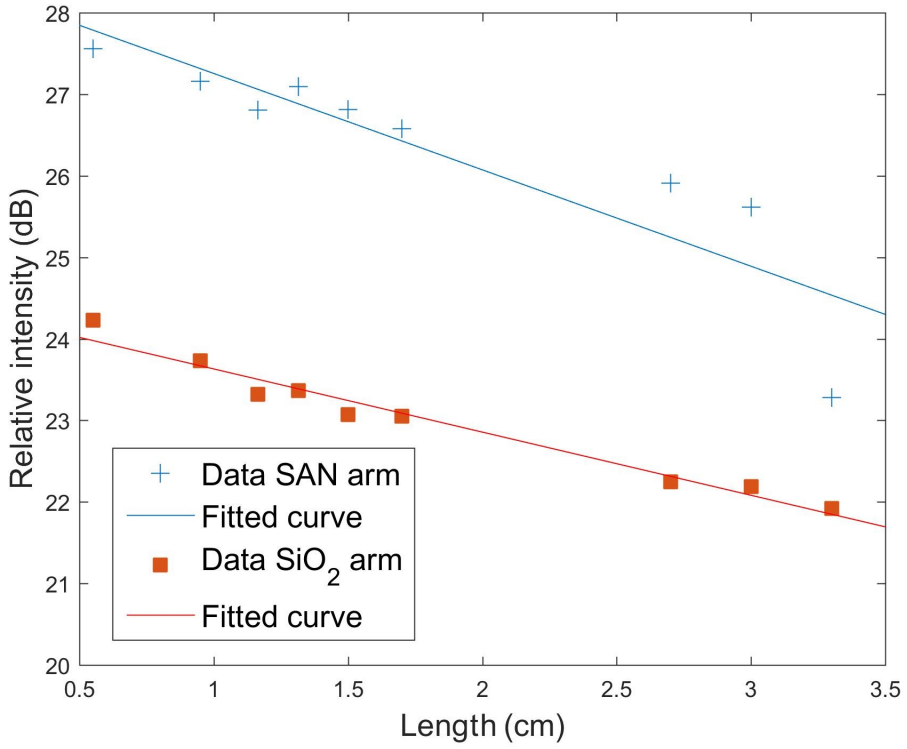

Figure 4.6: Relative intensity measured between the beginning and the end of the sensing window (Figure 4.5, area C), for a sensing arm and a reference arm.

still be measured along each arm. Losses are estimated to be 0.8±0.2 dB/cm and 1.0±0.2 dB/cm for the reference arm and the sensing arm, respectively.

Measurements were also done along the sensing arm before and after the sensing window (Figure 4.5, area B) and the whole chip before and after the splits (Figure 4.5, area A). This estimation is based on two points, to do any statistics more waveguides would have needed to be measured. Using the result, it can be estimated how much light is lost at the scattering points that occurs due to the beginning and the ending of the sensing window:

$$L_T = L_{Arm} + 2 \cdot L_{Sc} \tag{4.1}$$

where L_T is the total loss in the sensing arm, L_{Arm} is the loss in the sensing

window and L_{Sc} is the loss from the scattering points. Using Equation 4.1, the total loss of 7.3 dB and 1.0 dB/cm over the 3 cm length of the sensing arm, the loss from the edges of the sensing was calculated to be 2.1 dB.

The measurement allowed us to estimate the splitting ratio at the Y-junction, which which was found to be 46% to the reference arm and 54% to the sensing arm. These numbers are strongly dependent on the in-coupling.

Chapter 5

Measurements of sensitivity

In the chapter, the experimental results are presented. The sensitivity to temperature, pressure and methane is measured and compared to the theory from chapter 2. Further, both time-responses and LODs of the system was investigated.

5.1 Temperature sensitivity

As mentioned in chapter 1, the high sensitivity of a waveguide interferometer comes with the cost of high sensitivity to other parameters than the measurand and ambient conditions. To study the temperature sensitivity of the waveguides interferometers, I joined Firehun Tsige Dullo in the lab. Both asymmetric and symmetric waveguides were investigated for different sensing materials. Due to Dullo's previous work [14], it was chosen to continue with an Ytterbium fiber laser (IPG Photonics, 1070 nm, TE-Polarization). For experimental work, a waveguide Young interferometers was used, and temperature steps were applied with the Peltier element. My contributions to the paper includes, either alone or in collaboration with Firehun, all measurement on symmetric and asymmetric interferometers, except the result for oil on a asymmetric Young interferometer. Fig. 4 in the paper is an example of data I contributed with, and analyzed for the paper.

To investigate the effects of local changes in temperature, dynamic

and stationary simulations were carried out by Olav Gaute Hellesø and Svein Ketil Jacobsen. The measurements showed that an asymmetric interferometer is highly sensitive to uniform temperature changes, while a symmetric interferometer is almost insensitive to this. On the other hand, the numerical simulations showed that a symmetric device can be sensitive to asymmetric heating. More detailed results are presented in the paper, which is enclosed in Appendix B. The paper is also cited elsewhere in this thesis as [17].

5.2 Pressure sensitivity

In this section, interferometers with nitrogen and SAN as sensing media have been both theoretically investigated and experimentally tested for changes in pressure. All measurements have been done on 2 cm long waveguides, so that the MZI and the Young interferometer could be compared. Since the system used to regulate the pressure was new, the use of an Young interferometer was useful to see that phase change due to pressure was actually measured and not change due to mechanical shifts (section 1.4). For this and the coming sections, the experimental setup used is described in chapter 3.

For pressure measurements, a flow of 100 ml/min nitrogen was kept stable through the micro fluid chamber. The pressure was then set and regulated by the the pressure controller and a pressure meter was employed to read the pressure independently. For measurements with nitrogen, a clean chip without any materials on top was used. For measurements with SAN, SAN was spin-coated on top of the chip according to section 3.6. Nitrogen and SAN was investigated on a Young interferometer, while on the MZI, only SAN was investigated. Simulations of the phase change as a function of pressure were done in COMSOL (5.1) by Olav Gaute Hellesø, according to Equation 2.4 and using linear pressure dependency and values from Table 2.1 and Equation 2.12.

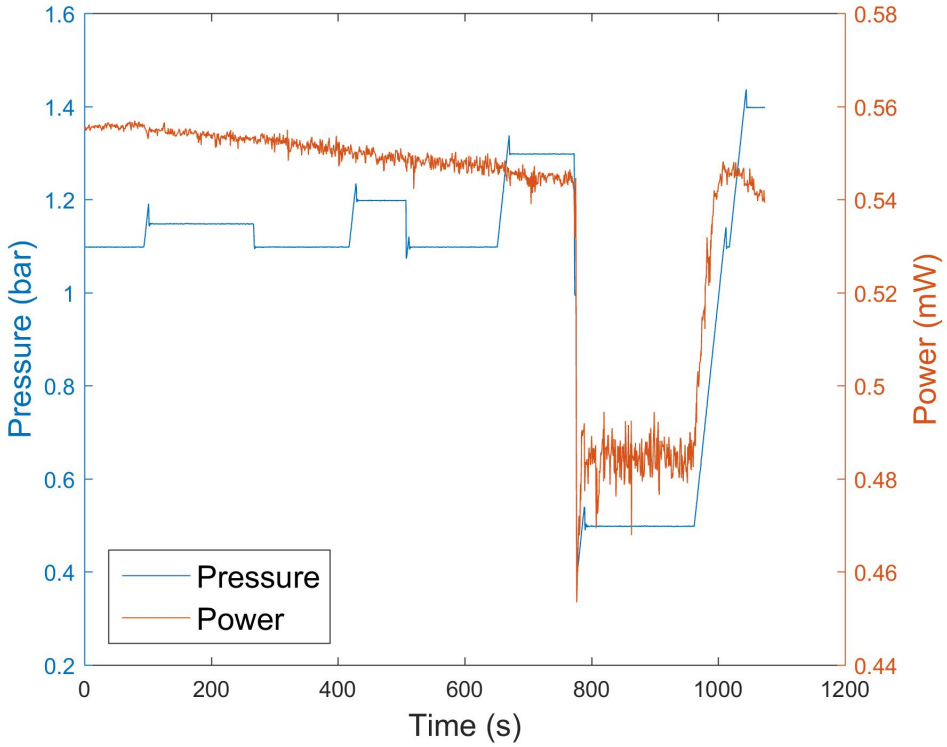

Figure 5.1: Output power from a straight waveguide while pressure is changed, with values both above and below 1 atm included.

5.2.1 Pressure on straight waveguides and symmetric interferometers

Experimental tests with straight waveguides and symmetric interferometers (2SW) were done to determine the stability of the system. First, light was coupled into a straight waveguide and the output power was measured while changing pressure. As seen in Figure 5.1, for changes in pressure over 1 atm (1 bar), the power is unchanged, but when the pressure goes below 1 atm (0-1 bar), the power changes. This effect is attributed to low pressure partially lifting the chip. Therefore, it was decided to only use overpressure ($>$ 1 atm) for measurements where pressure was the changing parameter.

Figure 5.2 shows a longer test where only overpressure has been applied. When reducing the pressure, the pressure controller drops the pressure

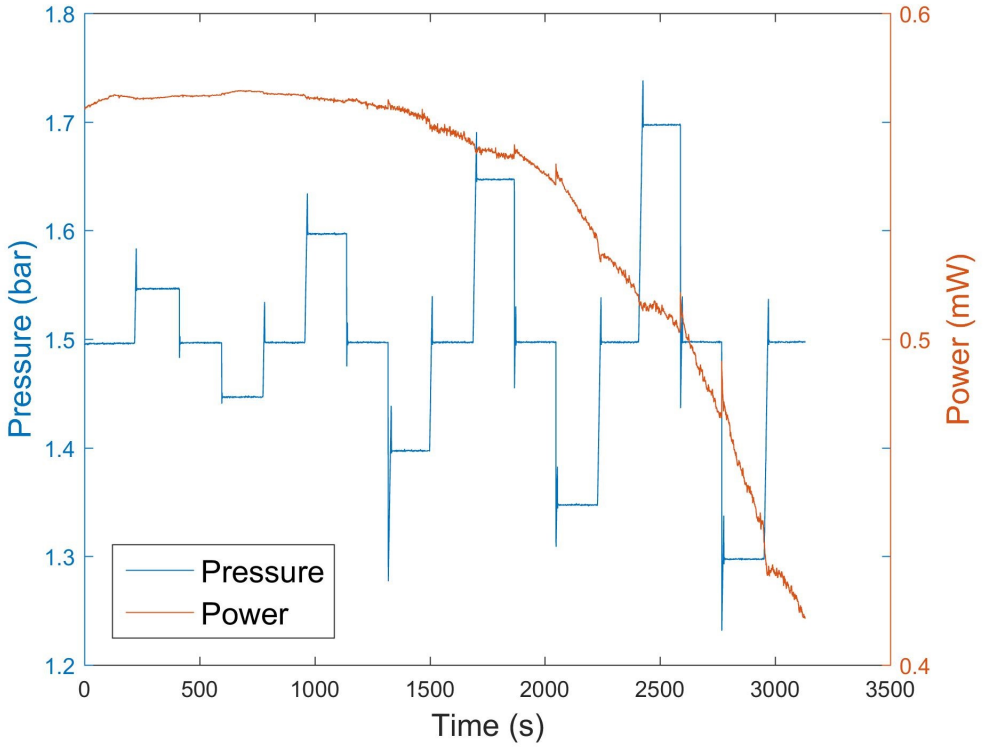

Figure 5.2: Output power from a straight waveguide when the pressure is cycled periodically over 1 atm.

quickly. This might create a shock-wave through the system. This effect is also seen at time after 1000 seconds in Figure 5.2. As long as the waveguide is well coupled (0-1000 s) this shock wave does not seem to affect the signal much.

A Young interferometer separates changes in phase from changes in amplitude, but a movement in the lateral direction will move the fringes horizontally in the same way as a change in phase. In Figure 5.3 the lateral position of the output beam from a straight waveguide is shown. When pressure is changed, there should not be any change in the output position. However, a small drift of about 1 pixel in 500 seconds is observed. This might be due to thermal movement of the system.

Figure 5.4 shows the same measurement with a symmetric young interferometer. There seem to be a correlation between position and pressure,

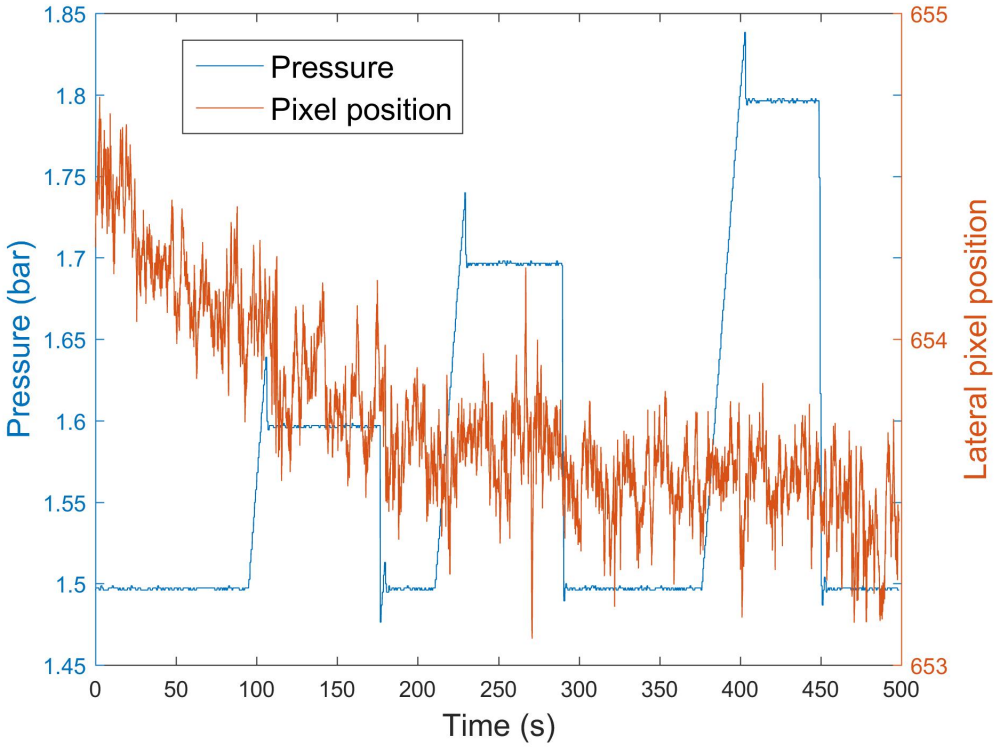

Figure 5.3: Lateral movement of a straight waveguide when the pressure is changed.

but the lateral movement is almost as small as the noise limit, a change of 0.4 bar gives about 0.5 pixel change. This effect might be from an inhomogeneous layer of SAN or a slight difference in the dimensions of the waveguide arms.

5.2.2 Pressure on asymmetric interferometers

Figure 5.5 shows the pressure and phase measured over time with a Young interferometer with SAN as cladding and TE mode. It is clear that the phase follows the pressure closely, and the phase vs. pressure dependency is shown in Figure 5.6. Figure 5.7 and Figure 5.8 show results for, respectively s, Young interferometer with nitrogen as cladding and a Mach-Zehnder interferometer with SAN as cladding in TE polarization. The slope and its uncertainty is shown in Figure 5.6-5.8, the offset is not shown because it is not important

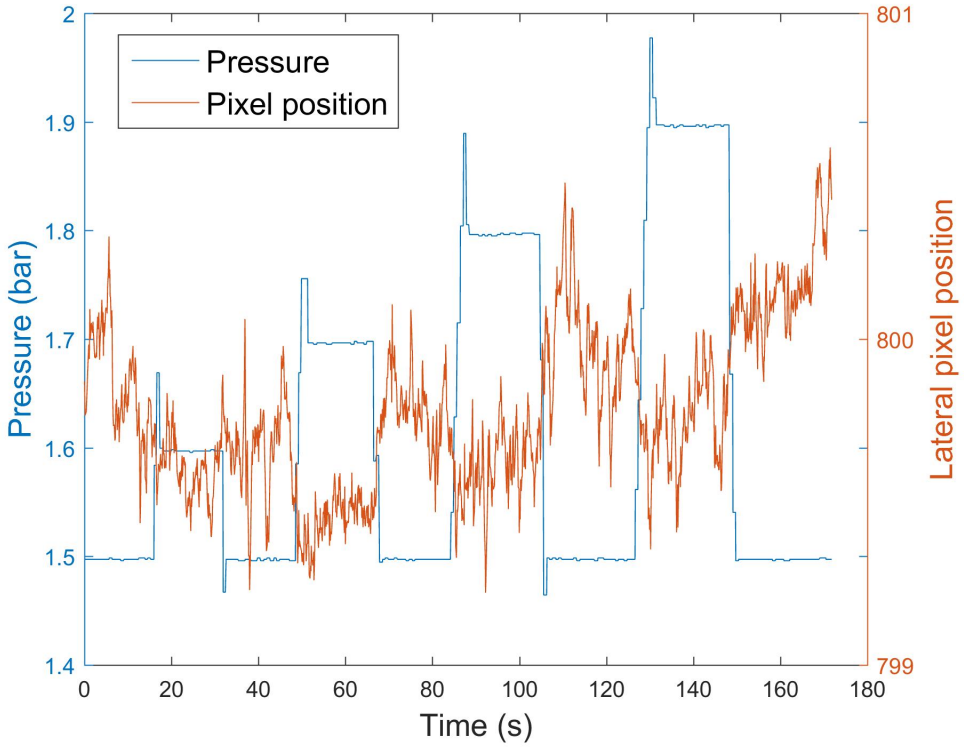

Figure 5.4: Lateral movement of a symmetric Young interferometer with SAN on both sensing arms when the pressure is changed..

for the result. The uncertainty of the slopes is based on the 95% confidence bound of the least mean square fit of the measured points and show that a linear fit is a very good approximation. The total uncertainty would also depend on uncertainties of the instrumentations, temperature variations, etc. and would thus be higher.

Table 5.1 shows results for the several interferometers and sensing media. For nitrogen clad Young interferometer, simulated results is show. The measured results is seen to be close to the simulated results. For the interferometers with SAN as sensing layer, since the refractive index dependency on pressure of SAN is unknown, simulations could not be done. In Equation 2.25, this dependency is given as a combination of compression and solubility of nitrogen in SAN. On the other hand, simulations could be done to find the refractive index dependency on pressure of SAN,

corresponding to the phase change measured, and was found to be $1.78 \cdot 10^{-5}$ RIU/bar.

On the basis of this simulation, an estimated range of the solubility of nitrogen in SAN could be found. At the high end, no compression is happening, hence the $\mathrm{d}n_{\mathrm{SAN}}/\mathrm{d}P$ in Equation 2.25 is equal to 0 and $S = 0.066$. At the low end, the solubility can no be smaller than 0.

To my knowledge, the solubility coefficient is not known for nitrogen in SAN. Van Krevelen et al. [50] compared the solubility of O_2, N_2, CO_2, and H_2 in 23 different polymers (SAN not included) and found the range for N_2 to be 0.02-0.081. Hence, the found range of 0 to 0.066 is a probable value.

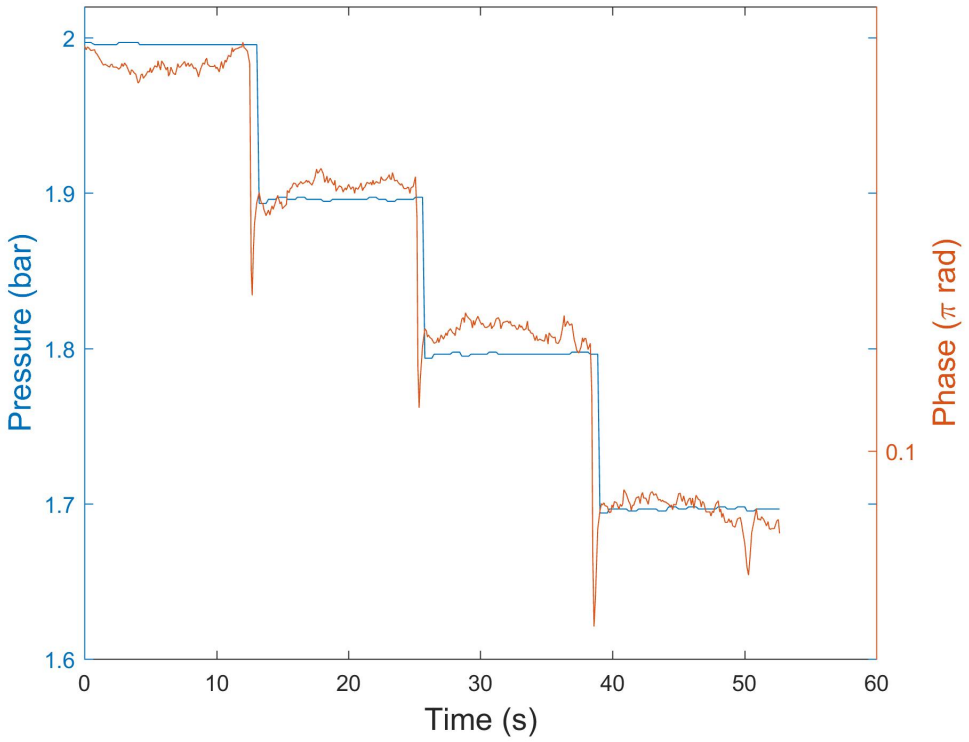

Figure 5.5: Applied pressure and measured phase for a Young interferometer with SAN as sensing medium (TE polarization).

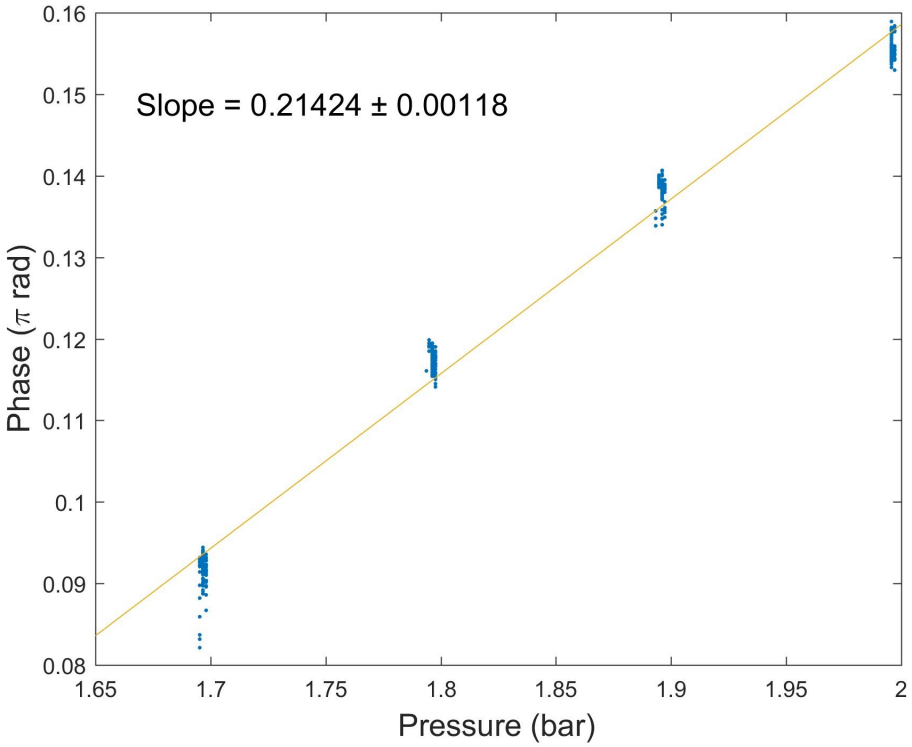

Figure 5.6: Measured phase as function of pressure corresponding to Figure 5.5.

Table 5.1: Measured pressure sensitivity vs. simulated values of asymmetric Mach-Zehnder and Young interferometers.

Interferometer	Mode	Sensing	Reference	Measured (π/bar)	Simulated (π/bar)
Young	TE	Nitrogen	Silica	0.887	0.884
Young	TM	Nitrogen	Silica	1.084	1.208
Mach-Zehnder	TE	SAN	Silica	0.208	-
Young	TE	SAN	Silica	0.214	-
Mach-Zehnder	TM	SAN	Silica	0.394	-
Young	TM	SAN	Silica	0.396	-

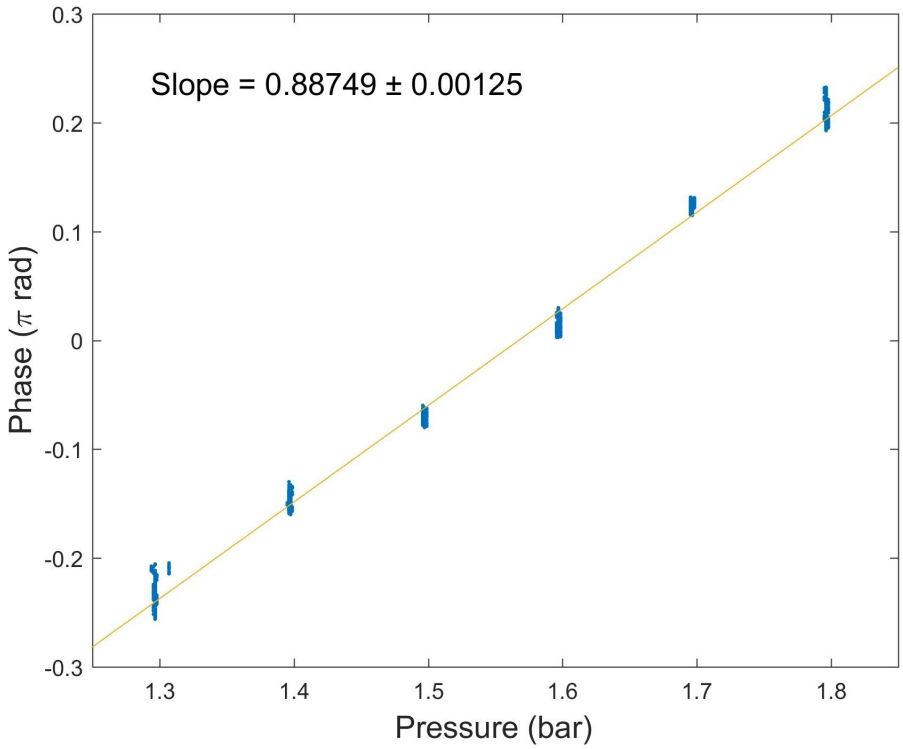

Figure 5.7: Measured phase as a function of pressure on a nitrogen clad asymmetric Young interferometer (TE polarization).

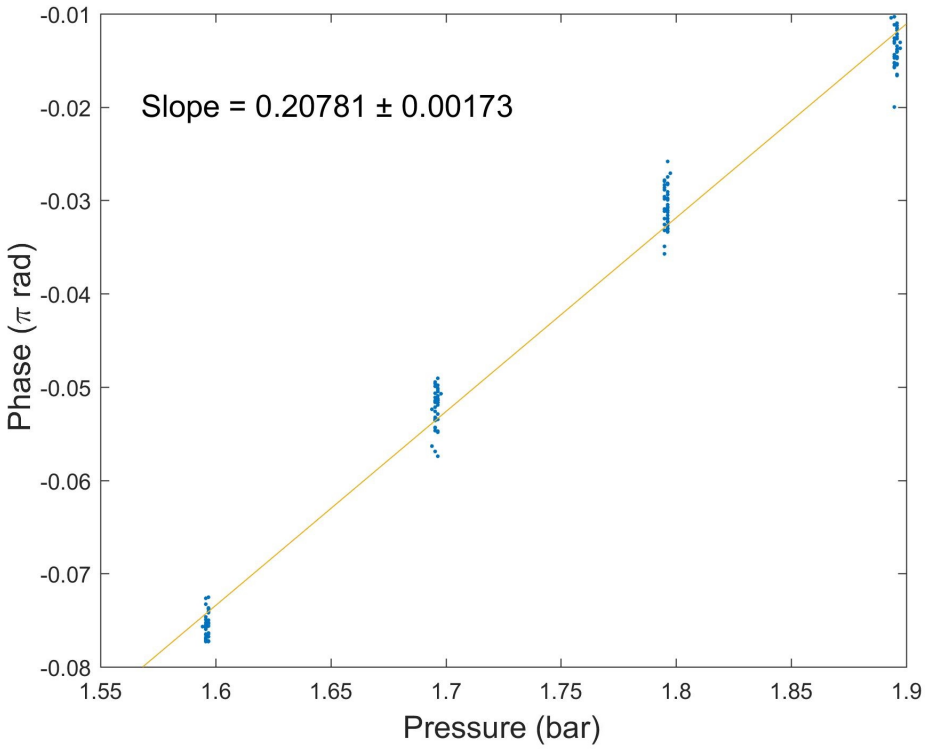

Figure 5.8: Measured phase as a function of pressure on a SAN clad asymmetric Mach-Zehnder interferometer (TE polarization).

5.3 Methane sensitivity

In this section, the sensitivity of SAN to concentrations of methane in nitrogen is investigated at various pressures. The diluted gas dissolves into the polymer, giving a change in refractive index based on concentration. This section will used as a reference to the enhancement in sensitivity due to cryptophane-A.

The phase change due to concentration of methane was measured with a Young interferometer for both TE and TM polarization at different pressures. Measurements were also done with a Mach-Zehnder interferometer, giving the same results as with Young interferometer. Thus, only Young interferometer is shown in this section.

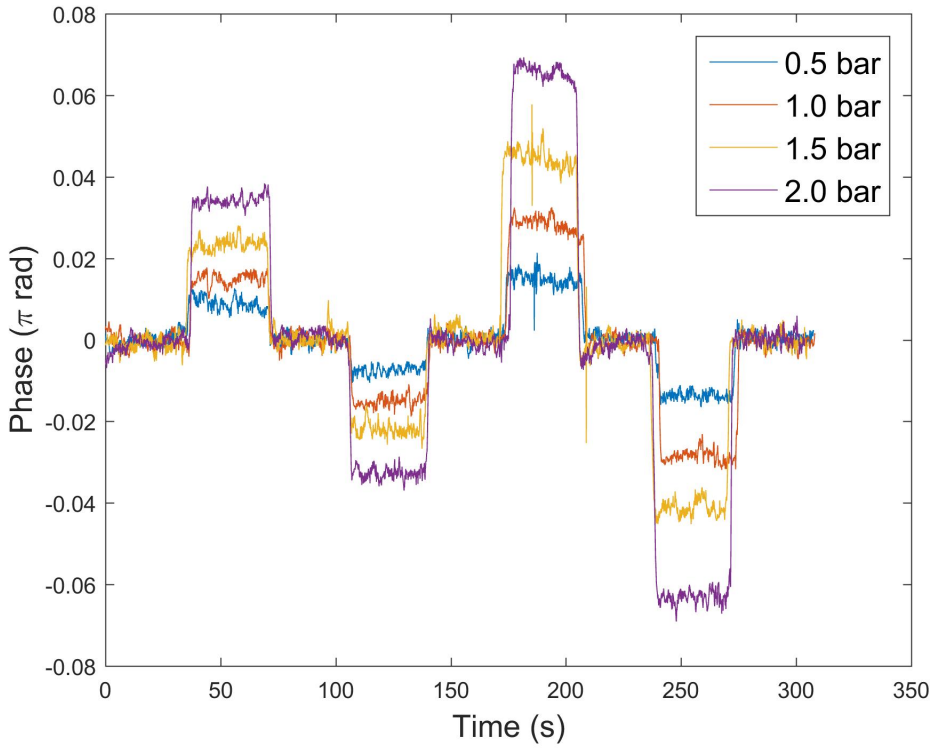

Figure 5.9: Measured phase for TE mode Young interferometer with SAN as sensing medium for different pressures when changing the concentration of methane.

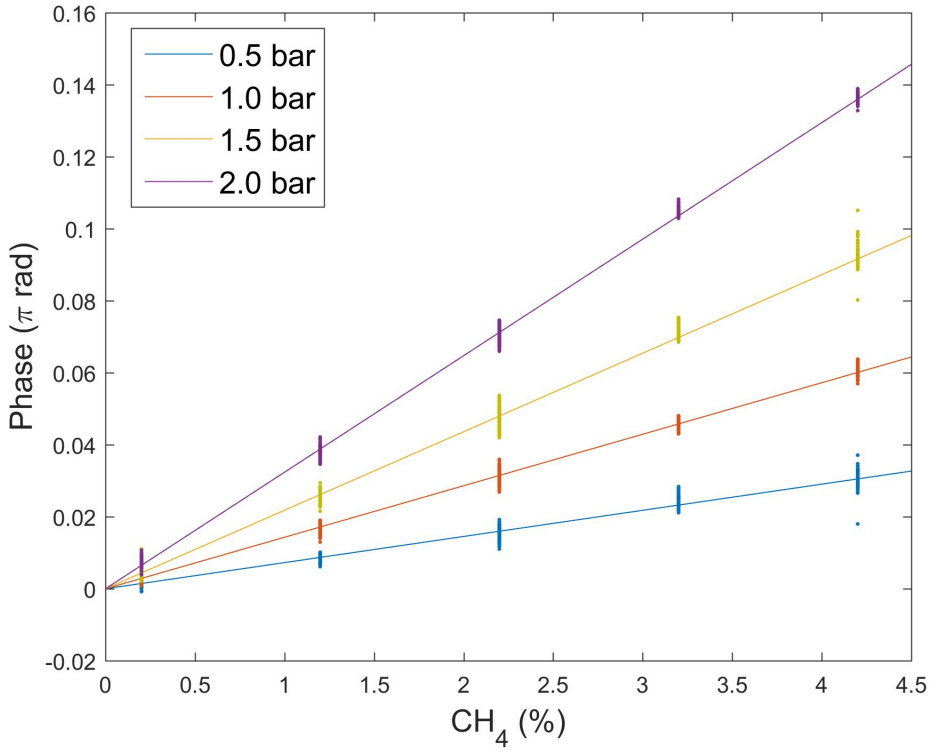

Figure 5.10: Phase as a function of concentration of methane corresponding to data from Figure 5.9.

For measurements, two flow controllers, both with range 0-100 ml/min, were used to control the flow and the concentration by having one MFC connected to pure nitrogen and the other MFC to 4.4 mol % methane in nitrogen. The concentration of methane was set to 2.2%, and cycled up and down with increasing step of 1% and 2%.

Since nitrogen and methane don't penetrate in silica and silicon nitride, Equation 2.8 can be written as:

$$\frac{\mathrm{d}\varphi}{\mathrm{d}x} = \frac{2\pi L}{\lambda_0}\left[S_{\mathrm{SAN}}\frac{\mathrm{d}n}{\mathrm{d}x}\right] \tag{5.1}$$

with S_{SAN} being the homogeneous sensitivity for the SAN layer ($\mathrm{d}n_{\mathrm{eff}}/\mathrm{d}n_{\mathrm{SAN}}$) and $\mathrm{d}n/\mathrm{d}\% = 0.01\mathrm{d}n/\mathrm{d}x$, chosen for the simplicity of measuring concentration in percent. S_{SAN} has been simulated with FimmWAVE and

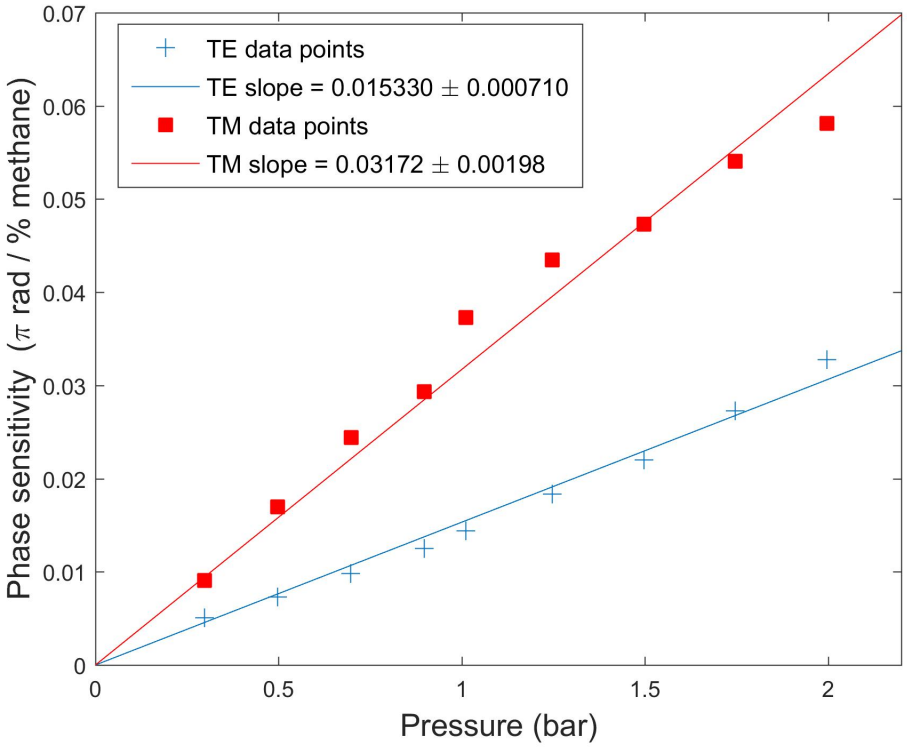

Figure 5.11: The methane sensitivity as function of pressure for both TE and TM polarization.

COMSOL to be 0.25 and 0.51 for TE and TM polarization respectively. Since dn/% is proportional to pressure, it is expected that the value of the slope when changing concentration also is proportional to pressure.

In Figure 5.9, the phase change is plotted for the same concentration steps for 4 different pressures. And in Figure 5.10, the corresponding slopes is seen. As seen, a higher pressure leads to a greater sensitivity towards methane. In Figure 5.11, the measured slopes at different pressures is plotted for TE and TM polarization, and a straight line is fitted through zero and the respective data points.

In subsection 5.2.2, the solubility of nitrogen in SAN was estimated in the range 0-0.066. Using this estimation, Equation 2.30 and the measured sensitivity, the solubility of methane in SAN is estimated in range of 0.30 to 0.35. The solubility of methane was measured for different silicone polymers

in Shah et al. [51], here solubility of methane is found to be in the range of 0.27 to 0.56.

5.4 Methane sensitivity enhancement due to cryptophane-A

Table 5.2: List of the different sensors with corresponding sensing layers and concentration of cryptophane-A to SAN.

Sensor	Doping	Concentration (c)
1	Cryptophane-A	1.6:45
2	Cryptophane-A	5.2:45
3	Cryptophane-A	14.2:45
Reference	Pure SAN (section 5.3)	-

In this section, three new sensors were made, as seen in Table 5.2, all with SAN doped with cryptophane-A as sensing layer, but with different concentration of cryptophane-A to SAN. The methane sensitivity of the sensors were investigated at different pressure. A fourth sensor is with pure SAN serves as a reference sensor. Sensitivity to methane and pressure dependency of the reference sensor have already investigated in section 5.3. During the measurement of the sensitivity to methane of sensors 1, 2 and 3, the pressure was kept stable and the concentration of methane was changed. This was then repeated for different pressures. Table 5.3 gives an overview of measurements preformed with the four different sensors. While sensor 1 was investigated at multiple polarizations, sensing lengths and different structures were measured, sensors 2 and 3 were only investigated for TM mode and 3 cm sensing length MZI as this gives the highest sensitivity. The concentration of methane was alternated in increasing steps between pure nitrogen (0%) and 1%. This can be seen in Figure 5.12, the orange line being the concentration, corresponding to the right y-axis.

In Figure 5.12, it can also be seen that there is a delay (6s) between the moment the MFCs are switched and the change in the methane concentration

Table 5.3: Table of what structures the different sensors is investigated at.

Interferometer	Young		Mach-Zehnder			
Sensing length	2 cm		2 cm		3 cm	
Polarization	TE	TM	TE	TM	TE	TM
Sensor 1	✓	✓	✓	✓	✓	✓
Sensor 2						✓
Sensor 3						1-2 bar
Reference	✓	✓	✓	✓		

is measured. This is the delay given by the volume of the tubing between the MFC and micro fluidic chamber, over the flow rate.

The blue line in Figure 5.12 shows the corresponding phase measured for sensor 2 at 1 bar. At the third step, 2500 ppm, and steps with higher

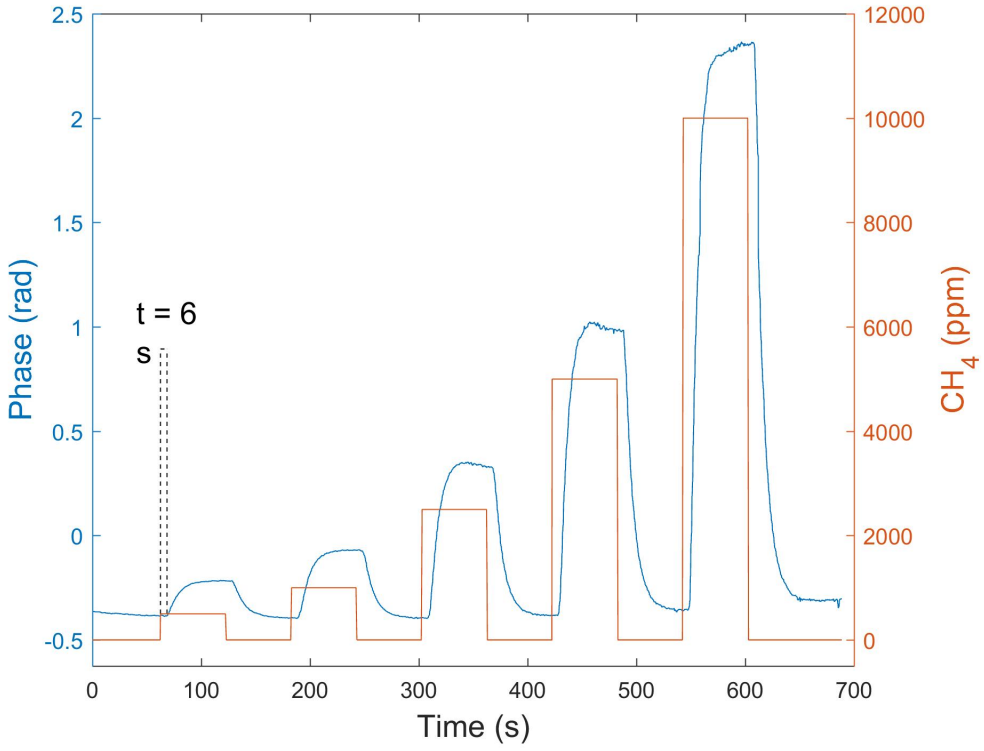

Figure 5.12: Measured phase change on sensor 2 at 1 bar (blue line) and corresponding concentration (orange line). The time is given from a change is done till it reaches the sensor.

concentration, the phase reaches a top and then falls down again. This is shown clearer in Figure 5.13, which shows the phase for sensor 2 at 2 bar with the same concentration steps. This effect was seen clearer at high pressures than low pressures, but still looks the same for all sensors with cryptophane. The methane concentration was then measured with a commercial Franatech TDLS sensor, and the measurement showed the same trend, hence, the effect is most probably originating from the MFCs or the gas flow system and not the cryptophane doped sensor itself. This has to be more closely investigated in the future.

The dotted lines in Figure 5.13 show were the values of the different phase is taken, giving a phase difference for the first three peaks. The four points, corresponding to 0 ppm, 500 ppm, 1000 ppm and 2500 ppm were used to

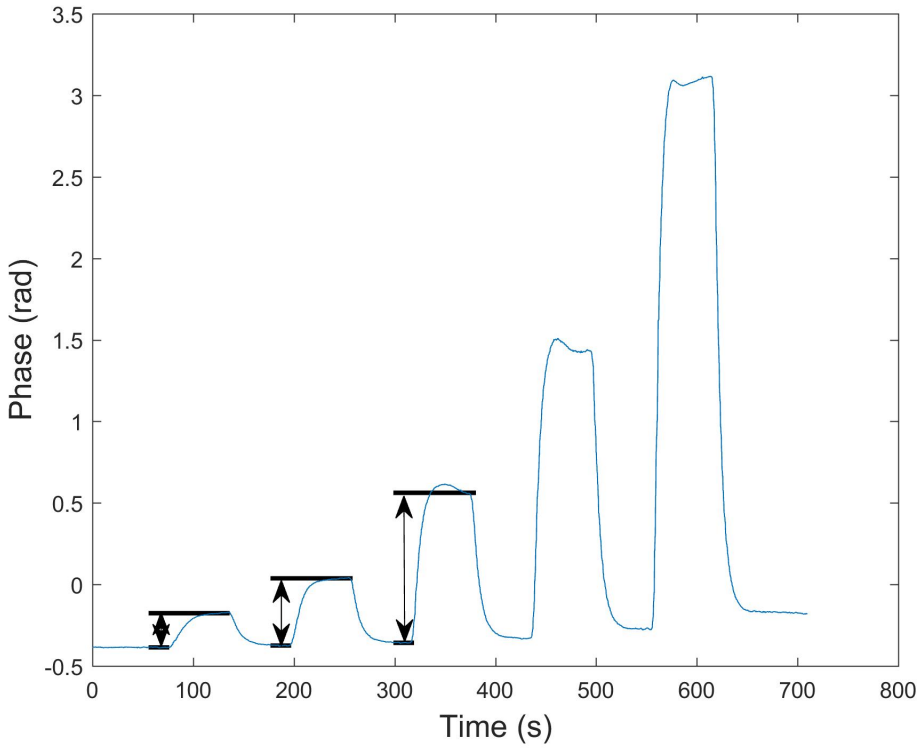

Figure 5.13: Measured phase change on sensor 2 at 2 bar corresponding to the concentration step as seen in Figure 5.12, with marked areas for data collecting.

calculate the sensitivity, $d\varphi/dppm$.

5.4.1 Sensitivity for MZI and Young interferometer and for 2 and 3 cm sensing lengths

Since sensor 1 was tested for both the MZI with 2 cm sensing length and the Young interferometer, the hypothesis that the phase change is equal for the two interferometers can be verified. The sensitivity of the two interferometers were measured at 8 different pressures. In addition, a point was inserted for 0 bar (vacuum) and 0 sensitivity because in vacuum there cannot be a concentration change. In Figure 5.14 the sensitivity is plotted against pressure for both MZI and Young interferometer at TE and TM polarization. As seen, both interferometers give very close results. Some

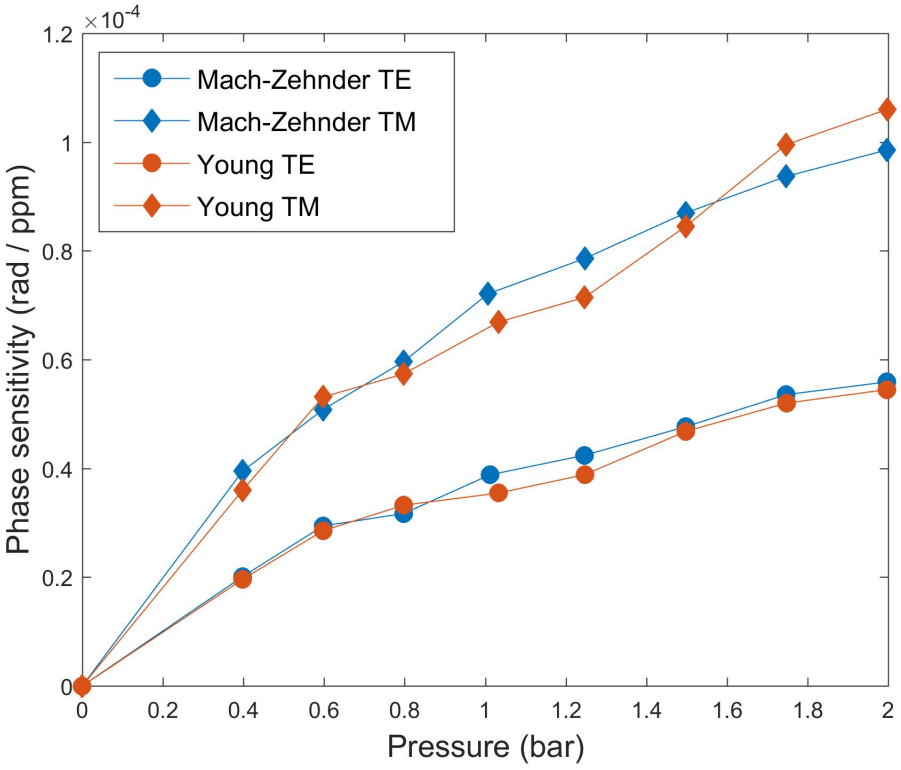

Figure 5.14: The sensitivity of sensor 1 as a function of pressure for both the MZI and the Young interferometer, and TE and TM polarization.

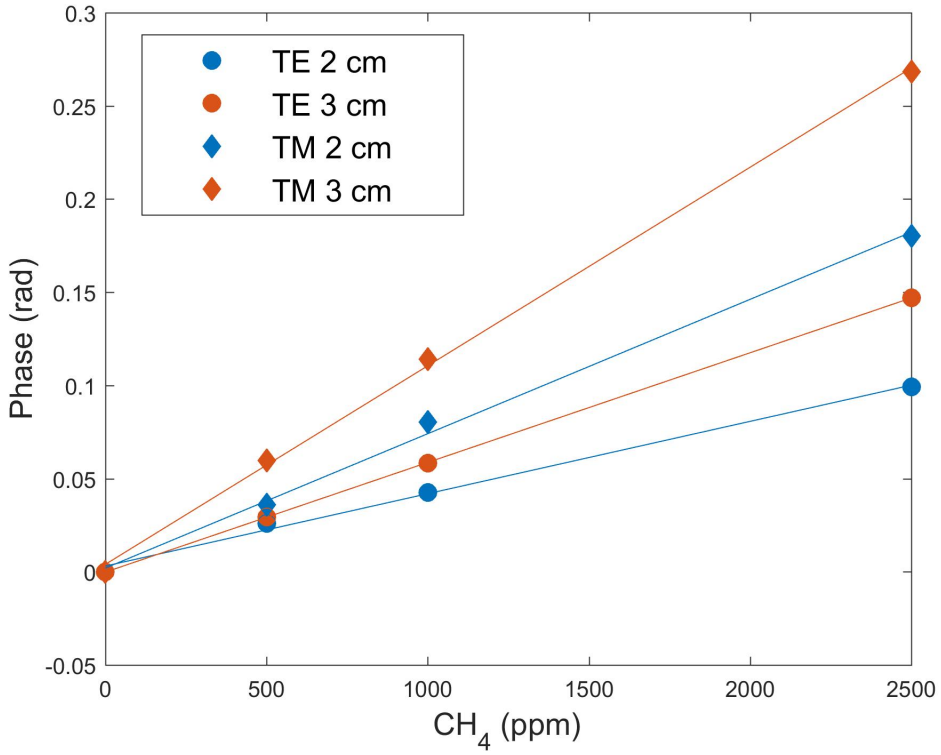

Figure 5.15: Phase change of sensor 1 as function of concentration of methane for a MZI with 2 cm and 3 cm sensing length, and TE and TM polarization.

offset is present, this might be from different drift during measurement, small dimension differences in the interferometers or differences in processing.

Further on, the investigation on MZI were done for TE and TM mode for both the 2 cm and the 3 cm sensing lengths. In theory, since the phase change is directly proportional to sensing length (Equation 2.1), the ratio should be a factor of 1.5. In Figure 5.15, the measured slopes for sensor 1 at 1 bar is shown for TE and TM mode at 2 cm and 3 cm sensing length. When taking the sensitivities of 3 cm divided by sensitivities for 2 cm for the respective polarizations and different pressures, the ratio between the 3 cm and the 2 cm sensing length was calculated to be 1.49 ± 0.04.

Figure 5.15 also shows that the TM polarization give higher sensitivity than TE polarization, this is because the field extends further into the claddings in TM mode, as seen in Figure 2.1. Therefore, for measurement

on sensor 2 and 3, only 3 cm sensing length for TM mode were investigated. The reference sensor was only measured for the 2 cm long sensing windows, but the assumption that a 3 cm sensing window gives 1.5 times bigger phase change is made.

5.4.2 Sensitivity at 1 bar

In Figure 5.16, the slopes of the sensors are shown at 1 bar, and the corresponding sensitivities are given in Table 5.4. As seen, the amount of cryptophane-A strongly changes the sensitivity of the chip. Sensor 3, which has the highest concentration of cryptophane-A, enhances the sensitivity by more than 50 times, compared to the reference sensor, without cryptophane-A. Further, in Figure 5.17, the sensitivities of the sensors are

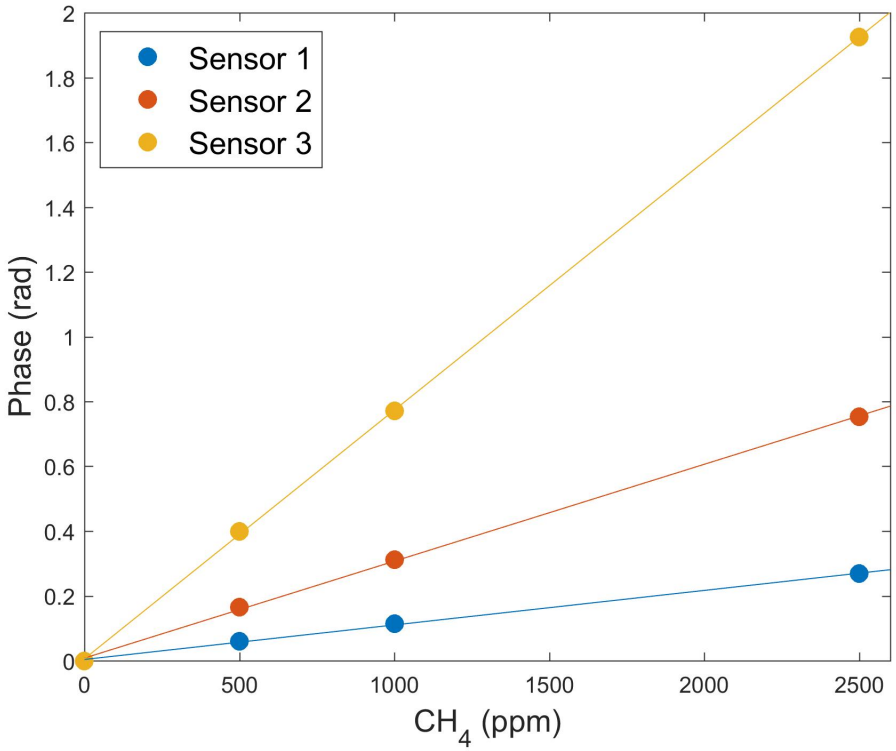

Figure 5.16: Phase change versus methane concentration for sensors 1 (blue), 2 (red) and 3 (yellow) at 1 bar.

Table 5.4: Measured sensitivity for the different sensors at 1 bar, and the enhancement in sensitivity compared to the reference sensor.

	Sensitivity (10^{-4} rad/ppm)	Enhancement
Sensor 1	1.06	7.1
Sensor 2	2.99	20
Sensor 3	7.68	51
Reference	0.15	1

plotted against the concentration, showing that the sensitivity is linearly dependent on the concentration.

Equation 2.33 described the phase sensitivity of cryptophane-A doped SAN:

$$\frac{\mathrm{d}n}{\mathrm{d}x} = 4.37 \times 10^{-4} S_{\mathrm{Pol,CH_4}} P - 2.68 \times 10^{-4} S_{\mathrm{Pol,N_2}} P + \frac{\partial F\left(x, c, P\right)}{\partial x} \qquad (2.33)$$

Since the result shows that the trapping of methane is linear with the concentration of methane, as seen in Figure 5.16, the derivative of the function $F(x, c, P)$ with respect to the concentration of methane (x) is constant. Hence, $F(x, c, P) \propto x$. Also, since the sensitivity is linearly dependent on the concentration of cryptophane (c), the function F is also proportional to the concentration c.

5.4.3 Pressure dependency

To test the effect of pressure on the sensitivities of the sensors, the sensitivities were measured at different pressures. In Figure 5.18, the sensitivities of sensors 1, 2 and 3 are plotted against pressure. Sensor 1 and 2 were tested over the range of 0.4-2 bars, which corresponds to the range of the pressure controller. Sensor 3 was tested only for overpressure, due to the much larger time response for this sensor as seen in subsection 5.4.4. Due to the long measurement time for sensor 3, the drift in the system and loss in amplitude due to coupling change that was produces at lower pressures, were hard to compensate for. Further, it is seen that the sensors are more sensitive at higher pressures, but the dependency is not linear as in the case of the

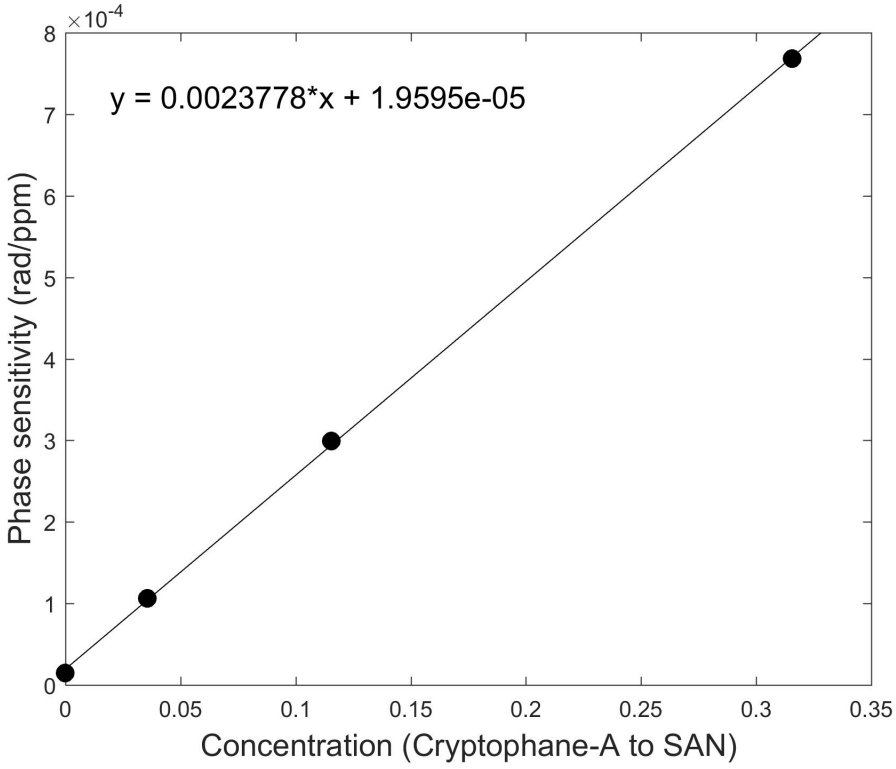

Figure 5.17: The sensitivities of the different sensors at 1 bar as function of the concentration of Cryptophane-A.

reference sensor.

Based on the results, an empirical formula for the sensitivity can be introduced. Since the change in phase is given as:

$$\frac{\mathrm{d}\varphi}{\mathrm{d}x} = \frac{2\pi L}{\lambda_0}\frac{\mathrm{d}n_{\mathrm{eff}}}{\mathrm{d}n}\frac{\mathrm{d}n}{\mathrm{d}x} \tag{5.2}$$

with $\mathrm{d}n_{\mathrm{eff}}/\mathrm{d}n$ found by simulations to be 0.51 for SAN as sensing medium and TM polarization, and $\mathrm{d}n/\mathrm{d}x$ given by Equation 2.33. For simplicity the concentration is chosen to be in ppm, where $\mathrm{d}n/\mathrm{d}ppm = 10^{-6}\mathrm{d}n/\mathrm{d}x$. For small concentration of cryptophane-A, it is assumed that the polymer can be assumed as SAN, with SANs properties, and for larger concentrations, as in sensor 2 and 3, the function F is the dominant term. Hence, Equation 2.33 is written as:

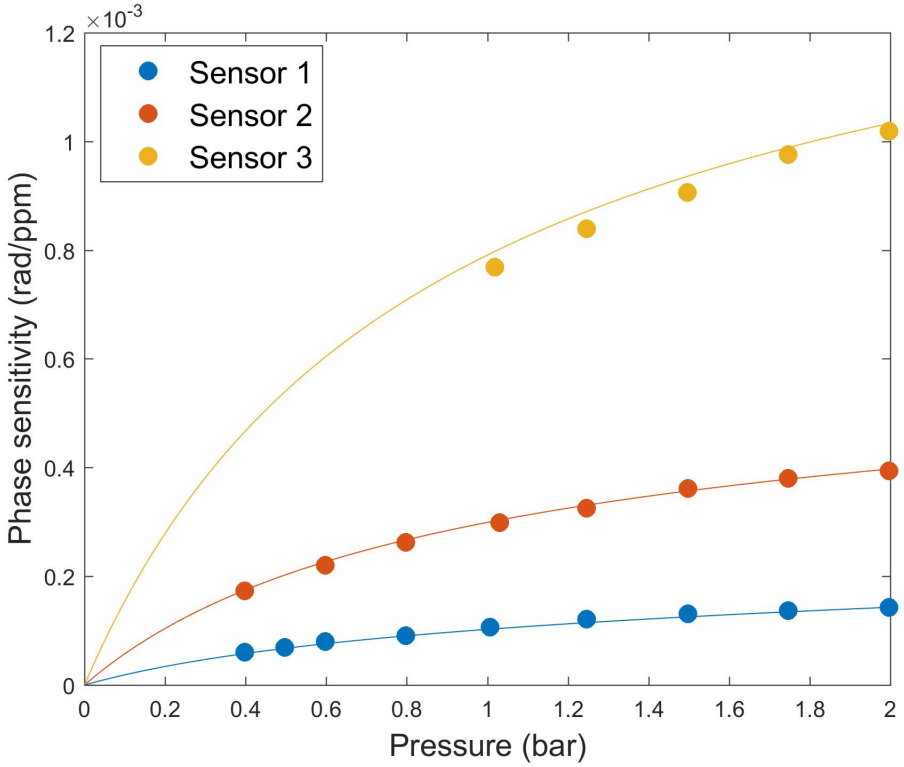

Figure 5.18: The sensitivity for sensors 1 (blue), 2 (red) and 3 (yellow) as a function of pressure with fitted curves given by Equation 5.4.

$$\frac{\mathrm{d}n}{\mathrm{d}x} = \left(\frac{\mathrm{d}n}{\mathrm{d}x}\right)_{\mathrm{SAN}} + \frac{\partial F\left(x, c, P\right)}{\partial x} \tag{5.3}$$

where $\mathrm{d}n/\mathrm{d}x$ is given by the reference sensor. MATLAB was used to find the best fit of the points in Figure 5.18 and an empirical formula was found to be:

$$\frac{\mathrm{d}\varphi}{\mathrm{d}ppm} = 0.15 \cdot 10^{-4} P + \frac{0.0045cP}{P + 0.83} \tag{5.4}$$

where P is the pressure and c is the concentration of cryptophane-A in SAN. Equation 5.4 is plotted in Figure 5.18 for the corresponding concentrations of cryptophane-A. As seen, the formula seem to be a good fit. Since the formula is empirical, it does not say anything for pressures over 2 bar or higher concentration of cryptophane-A to SAN. For the latter one, sensor 3 is probably on the limit of how much cryptophane-A that can be solved in

SAN. When it comes to pressure, Equation 5.4 predicts that when increasing the pressure that the contribution form the cryptophane-A will becomes close to negligible.

5.4.4 Time-response

A common way to define the response-time of a system is to measure the time it takes to go from 10% to 90% of the full change, also called rise-time, t_{10-90}. The time-responses were measured for the three sensors and the reference sensor at different pressures, and were found independent of pressure. The time-responses were also measured to be the same for different concentration steps of methane, but might be dependent on the thickness of the polymer layer. The thickness of the polymer layers are assumed to be the same due to the same procedures when deposing them on the chip (section 3.6), and with a thickness of about 1 µm, the effect of thickness for response-time could not be investigated. Hence, time-response is here only given as a factor of the concentration of cryptophane-A. In Figure 5.19, the phase change corresponding to a change of 1000 ppm is plotted for sensor 1, 2 and 3, and the corresponding time responses are shown. As seen, the time it takes for sensor 3 to settle is much longer than for sensors 1 and 2. The time-response of the different sensors is given in Table 5.5, and in Figure 5.20 the various time responses are plotted against the concentration of cryptophane-A. An exponential fit is made to relate the time-response with the concentration of cryptophane-A:

$$t = 35 \exp\left[3.6c\right] - 33 \tag{5.5}$$

Equation 5.5 seems to be a good approximation of the response-time. While the sensitivity of the sensors is increasing linearly with increasing concentration of cryptophane-A, the time-response is increasing exponentially. Hence, increasing the sensitivity by increasing the concentration of cryptophane-A comes at the expense of a longer response-time.

Table 5.5: The measured t_{10-90} time response for the different sensors.

	Concentration (c)	t_{10-90} (s)
Sensor 1	1.6:45	7.5
Sensor 2	5.2:45	20
Sensor 3	14.2:45	75
Reference	-	2.0

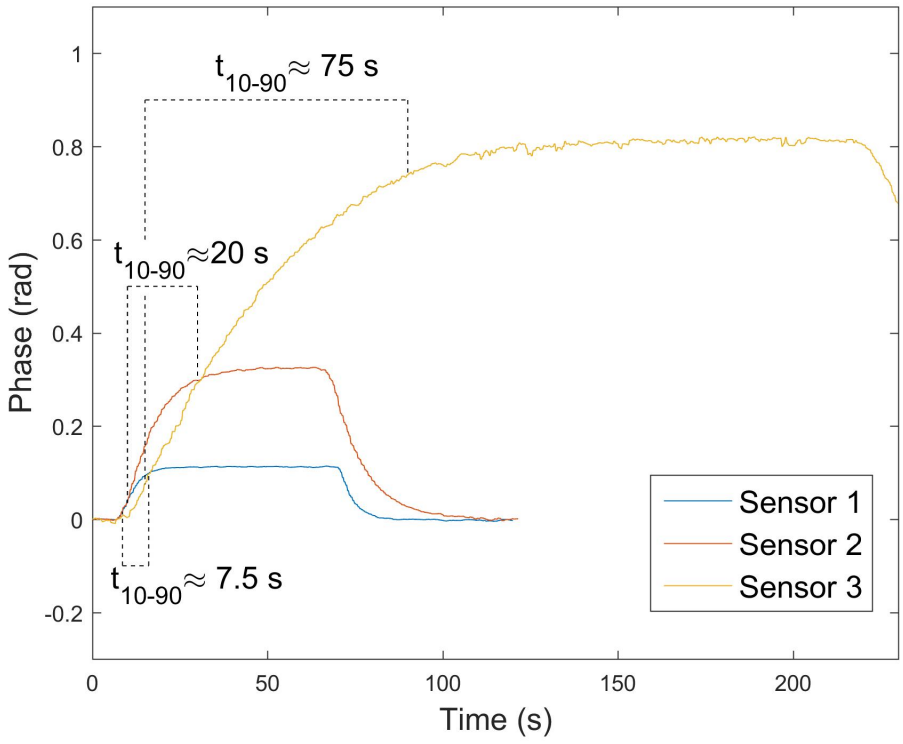

Figure 5.19: A phase step when a concentration change of 1000 ppm methane is applied to sensor 1 (blue), sensor 2 (orange) and sensor 3 (yellow), and the corresponding t_{10-90} response time.

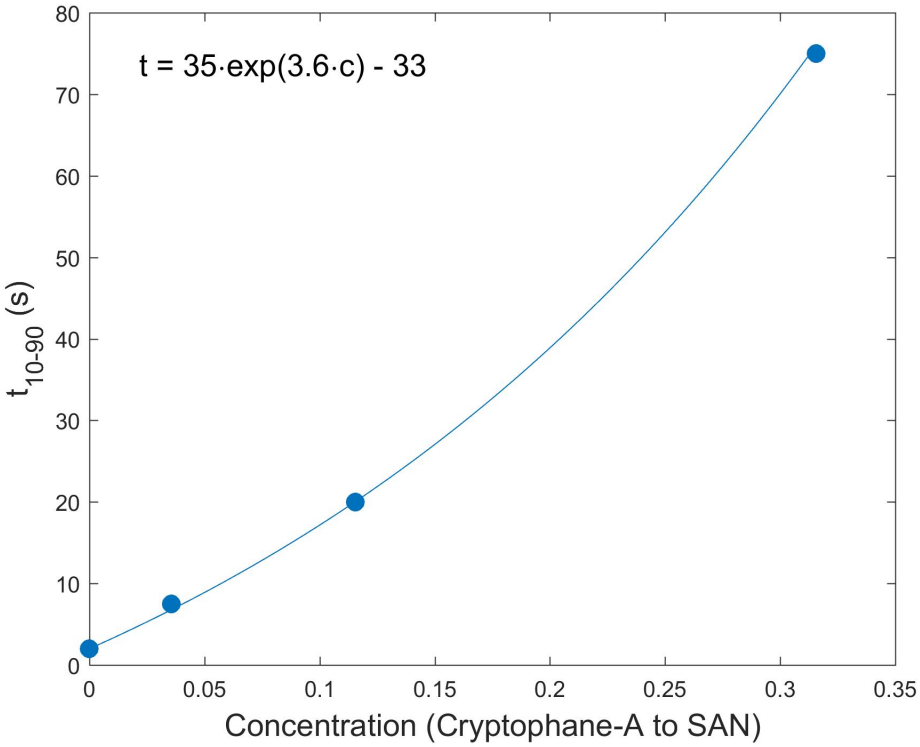

Figure 5.20: The time response plotted as a function of cryptophane-A concentration.

5.4.5 Limit of detection

The limit-of-detection is the lowest amount of methane the sensor can measure. Hence, to know the LOD is one of the most important properties of the sensor. The LOD was calculated according to procedures suggested by the American Chemical Society [52, 53] to a 99% confidence level. The results from this section are also used and published by Dullo et al. [8]. The LOD is given as:

$$\mathrm{LOD} = \frac{2.821\sigma_y}{S} \tag{5.6}$$

where σ_y is the standard deviation of the 10 repeated measurements close to the expected detection limit and S is the sensitivity of the sensor, $\mathrm{d}\varphi/\mathrm{d}ppm$.

First, measurement were done with nitrogen connected to both MFCs. When having one MFC without flow and repeatably turning on a small flow,

while the other MFC was flowing with high flow (corresponding to zero and small concentration of methane), a phase change was noticed. This change was only noticed when one of the MFC had been off for a while and always was used on a small flow-rate, typically flows corresponding to less than 300 ppm of methane concentration. This is assumed to be due to the different temperatures of the gases if one of the gases was staying in the tubing in front of the MFC, while the other was flowing. To correct for this, shorter tubes were put between the gas bottles and MFCs to minimize temperature differences. For measurements where small concentrations of methane was used, as for LOD measurements, a third MFC was added to the system, working as an overflow valve to keep the flow in the methane tubing the same as in the nitrogen tubing. A mixing chamber was also put between the MFCs and the micro fluidic chamber to better homogenize the gas temperature before the sensor. After these improvements, measurement with nitrogen connected to both MFCs did not show any phase change, even when using small flow-rates on one of the MFCs.

The standard deviation was found according to [53], by cycling the concentration between 0 and 300 ppm 10 times, as seen in Figure 5.21, and taking an average of the last 15 seconds of each cycle. Hence, 10 different steps were acquired for a 300 ppm concentration change. The standard deviation was then found from:

$$\sigma_y = \frac{1}{N-2} \sum_i (y_i - \bar{y})^2 \tag{5.7}$$

where y_i is the measured step-sizes and $\bar{y}$ being the mean step-size. The standard deviation was measured only for sensor 1, but assumed to be the same for all sensors. The result gave a $\sigma_y = 1.65 \times 10^{-3}$, which correspond well to the noise level found in section 4.1. In Table 5.6, the calculated LODs using the slopes previously found and Equation 5.6 at 1 and 2 bar, is shown.

From Equation 5.6, it is given that the LOD is inverse proportional to the sensitivity. Hence, increasing the sensitivity will decrease the LOD. But as seen in the previous sections; increasing the amount of cryptophane-A comes with the cost of high response-time, and increasing the pressure will

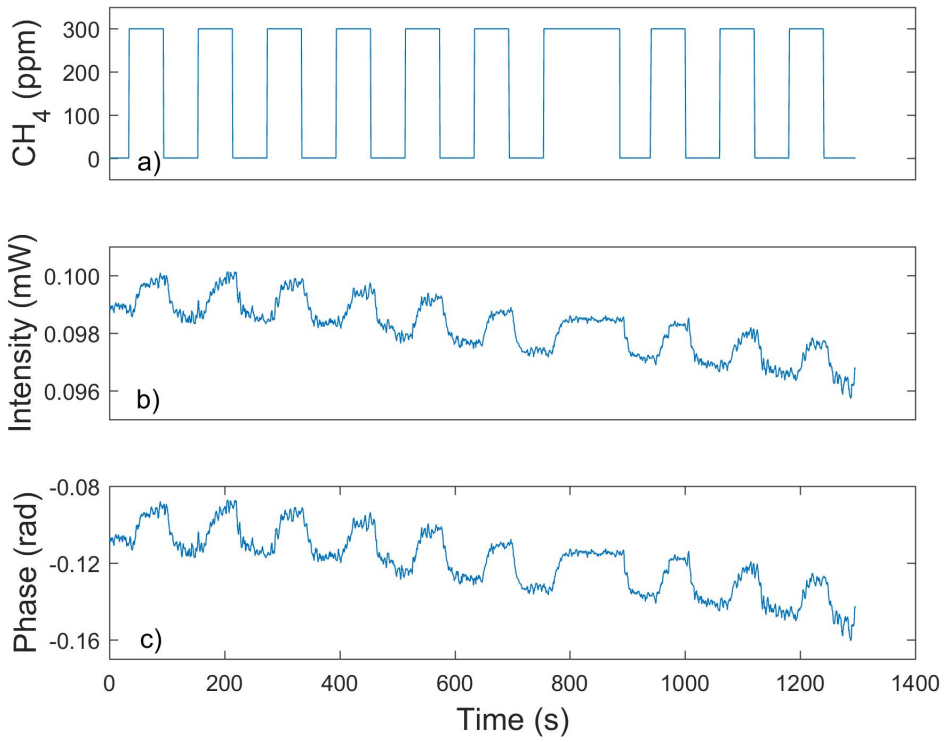

Figure 5.21: The methane concentration in the microfluidic chamber (a), the resulting output intensity (b) and the corresponding phase change (c), for measurements of σ_y.

Table 5.6: The calculated LODs for the different sensors at 1 bar and 2 bar.

	LOD (ppm)	
	1 bar	2 bar
Sensor 1	44	33
Sensor 2	16	12
Sensor 3	6.1	4.6
Reference	265	170

reduce the effect of using cryptophane-A, hence, reducing the selectivity of the sensor. The most effective way to decrease the LOD is thus to decrease the noise σ_y. Decreasing the noise can be done by reducing sensitivity to other parameters, like changes in temperature and pressure. Gluing a fiber to the chip will also reduce noise originating from the changes in the in-coupling. Another way to reduce noise is to use a faster DAQ, such that measurements can be taken at a higher rate, and hence, the signal can be averaged.

Chapter 6

Conclusions and future work

This thesis describes the use of cryptophane-A as a compound to enhance methane sensitivity. A cryptophane-A doped polymer is used as the sensing layer on a waveguide interferometer that is employed for methane gas detection. The sensing layer provides very high sensitivity and selectivity to methane.

First, a device with pure polymer as the sensing medium was investigated for methane sensitivity, at different pressures. The results showed a moderate sensitivity to methane, which linearly increased with pressure. But this sensitivity is assumed to be non-selective, i.e. all gases that can diffuse into the polymer layer will give a phase change.

Second, polymer doped with cryptophane-A was used as the sensing medium, resulting in an increase sensitivity of more than 50 times relative to the sensor without cryptophane-A. Furthermore, the sensitivity was shown to be directly proportional to the concentration of cryptophane-A. This gave, for sensor 3, a limit-of-detection of 6 ppm at 1 bar and 4.6 ppm at 2 bar, which is the best LOD reported with this configuration, 3 times lower than what reported by Dullo et al. [8]. But the high sensitivity comes of the cost of longer response-time, the most sensitive sensor resulted in a response time of 75 seconds. While the sensitivity is linearly proportional to concentration of cryptophane-A, the response-time is increasing exponentially. Hence, a compromise has to be made to get high sensitivity but still maintain a

reasonable response-time.

The cryptophane based sensors also showed increased methane sensitivity with increasing pressure. This dependency was described by an empirical formula:

$$\frac{\mathrm{d}\varphi}{\mathrm{d}ppm} = 0.15 \cdot 10^{-4} P + \frac{0.0045cP}{P + 0.83} \tag{5.4}$$

showing that increasing the pressure only results in a small increase in sensitivity.

High-sensitivity can also give high sensitivity to other parameters than the measurand. Therefore, temperature and pressure sensitivities were investigated. The measurement results show that a symmetric device, with the same material on both arms, is almost insensitive to uniform changes in temperature and pressure. While an asymmetric device, with different materials on the arms, is highly temperature and pressure sensitive. However, numerical simulations revealed that a symmetric device can be sensitive to asymmetric heating of the top surface.

To further improve the device, the high sensitivities to other parameters, like temperature and pressure, have to be reduced. One way of doing this is to use a cryptophane-A doped polymer on one of the arms and the same polymer, but without cryptophane-A, on the other arm. In this scenario, temperature and pressure changes will be compensated, making the interferometer insensitive to these parameters. Also, only phase change due to methane molecules trapped by cryptophane-A will be measured, making the device even more selective to methane.

The limit-of-detection of 5 ppm is a huge improvement compared to a sensor without cryptophane-A, but still 1-2 orders of magnitude higher than needed for ambient methane measurements. As already stated, increasing pressure will only give limited sensitivity increase, and increasing the cryptophane-A concentration will come of the expense of response-time. Hence, the most efficient way to improve the LOD would be to reduce the noise level.

In real-world applications, the Mach-Zehnder interferometer is preferred to the Young interferometer for several reasons: Even though the Young

interferometer can separate phase change from amplitude change, the use of a fiber glued to the chip, "pig-tailing the chip", will eliminate amplitude changes due to in-coupling. The Mach-Zehnder interferometer is also a much simpler device, since it only needs to measure power. Using a Young interferometer with a camera would also effect the size of the sensor, as well as the noise level due to inferior noise performance.

Appendix A

List of parts

A.1 Optical setup

Item	**Manufacturer**	**Id**
Optical table	Standa	1VIS95W
Laser	Crystal Laser	DL785-120-S0
Half-wave plate	Thorlabs	
Beam expander lens 1	Thorlabs	AC254-030-B-ML
Beam expander lens 2	Thorlabs	LA1986-A
Polarizer	Thorlabs	LPVIS100-MP
Objective lens input	Leitz Wetzlar	569244
Objective lens output	Olympus	UIS 2 PLN10X
Power detector	Thorlabs	SM1PD1A
Camera	Allied Vision	GC2450
Piezo translation stage	Thorlabs	MAX 302/M
Piezo controller	Thorlabs	MDT 693A
Modular Rack Chassis	Thorlabs	PRO8000
Photocurrent measurement card	Thorlabs	PDA8000-2

A.2 Chip and fluid system

Item	**Manufacturer**	**Id**
Peltier	Laird Technologies	430139-513
Temperature controller	Thorlabs	TED8080
MFC 100 ml/min x2	Bronkhorst	F-201-CV-100-AAD-11-V
MFC 0.7 ml/min x2	Bronkhorst	F-200-CV-002-AAD-11-V
Pressure Controller	Bronkhorst	P-702CV-6K0A-AAD-11-V
Pressure meter	Apisens	PCE-28
Vacuum pump	VWR	PM20405-86
Gas	AGA	Nitrogen
Gas	AGA	2.0 mol % CH_4 in N_2
Gas	AGA	4.4 mol % CH_4 in N_2

A.3 Microscope

Item	**Manufacturer**	**Id**
Objective lens	Olympus	UIS 2 PLN4X
Objective lens	Olympus	UIS 2 PLN10X
Camera	Ueye	UI-1240SE-M-GL
Light	Olympus	KL 1500 LCD
Part	Olympus	U-5RE-2
Part	Olympus	U-TLU
Part	Olympus	U-TVI X
Part	Olympus	U-CMAD-2

Appendix B

Publication: Temperature sensitivity of a waveguide Young interferometer

Under review in Photonics Technology Letter.

Authors: Firehun Tsige Dullo, Martin Ingvaldsen, Jana Jágerská, Svein Ketil Jacobsen, and Olav Gaute Hellesø

Author contributions: Firehun Tsige Dullo did the experiments and wrote the draft of the paper. I contributed to the experimental work and commented on the paper. Jana Jágerská contributed to the thermo-optical model and revised the paper. Prof. Svein Ketil Jacobsen and Prof. Olav Gaute Hellesø did the simulations and revised the paper.

Temperature sensitivity of a waveguide Young interferometer

Firehun Tsige Dullo, Martin Ingvaldsen, Jana Jágerská, Svein Ketil Jacobsen, *Senior Member, IEEE,* and Olav Gaute Hellesø, *Member, IEEE*

***Abstract*—The temperature sensitivity of a waveguide Young interferometer is investigated experimentally and using numerical simulations. With different materials on the two arms of the interferometer, the output phase is linear with temperature, making the device suitable for on-chip temperature sensing. A symmetric interferometer with the same material on both arms is almost insensitive to hotspots and temperature steps applied to the bottom of the substrate, while it is still sensitive to asymmetric heating of the top surface. For biological or chemical sensing, it must be assured that any heating of the top surface, e.g. from liquid or gas flow, is symmetric with respect to the interferometer, both for asymmetric and symmetric devices. For a 20 mm long device, the difference in temperature between the two arms must be limited to a few mK in order not to influence the performance of the device.**

***Index Terms*—Optical waveguides, Young interferometer, Mach-Zehnder interferometer, temperature.**

I. Introduction

INTERFEROMETERS provide very high sensitivity with respect to optical pathlength, and indirectly to a range of physical, chemical and biological parameters. This comes at the expense of high sensitivity to ambient conditions and to other parameters than the measurand. Waveguide interferometers have the advantage of being integrated on a chip. They are thus less susceptible to mechanical vibrations and temperature changes than bulk or fiber interferometers. In addition, waveguide interferometers can be miniaturized and potentially mass-produced. The most studied waveguide interferometer is the Mach-Zehnder interferometer, notably for evanescent field biological and chemical sensing [1], [2]. The great advantage of the Mach-Zehnder interferometer is a reference arm running parallel to the sensing arm, which can reduce unwanted sensitivity. Special designs have been demonstrated to give low temperature dependency also with different lengths for the two arms [3], [4]. Asymmetric interferometers, with different claddings on the two arms, are studied in the first part of this work. With identical arms and cladding materials, a symmetric device should ideally not be sensitive to changes in the chip temperature. This will be studied experimentally and the results compared to the noise-level of the measurements. For these experiments, the entire chip is heated uniformly. To explore the effect of local changes in temperature, dynamic and stationary simulations are carried out. These simulations aim at showing worst-case scenarios and to show the difference between non-uniform temperature distribution below the chip and on the chip surface. Bad thermal connection to a chip holder can give hotspots below the chip, while the most likely source of non-uniform heating of the surface is flow in a microfluidic channel close to (one of) the waveguides. Whereas waveguide interferometers have been studied for many applications, experimental and numerical studies of the temperature influence on the devices are few, particularly for symmetric interferometers.

The Mach-Zehnder interferometer has a single output, while the Young interferometer gives a set of fringes, which makes it possible to separate changes in amplitude and phase [5]. Thermal effects of an asymmetric interferometer have been studied with the Mach-Zehnder configuration [6]. As thermal effects are significantly smaller for a symmetric interferometer, a Young interferometer is used in this work because it is less influenced by thermal changes of the incoupling. As both interferometers have closely spaced waveguide arms, the results are also valid for waveguide Mach-Zehnder interferometers.

II. Interferometer design and experimental setup

Optical waveguides were fabricated of silicon nitride (Si_3N_4) on oxidised silicon substrates. Shallow rib waveguides were made by wet-etching a 5 nm high, 2 μm wide rib into a 150 nm thick Si_3N_4 core. The waveguides were covered with a 1 μm thick silica cladding and 20 mm long sensing windows were etched down to the waveguides. The fabrication process was as detailed in ref. [7]. In a Young interferometer, a Y-junction splits a single-mode input waveguide in two waveguide arms (Fig. 1). Towards the end of the chip, the arms are expanded, giving two inclined, tapered sections, which give interference fringes on the output facet of the chip. The chip contains interferometers with a sensing window on both waveguide arms and interferometers with a sensing window on only one arm. The second arm is thus covered with silica and acts as a reference arm. For the experiments, the chip, and thus all sensing windows, was covered by air, oil (refractive index liquid, Cargille Labs) or a polymer. The polymer used was styrene-acrylonitrile (SAN, Sigma-Aldrich, 25 wt. % acrylonitrile). It was prepared by dissolving pellets of SAN (45 mg) in 0.9 mL of 1,1,2,2-tetrachloroethane and spin-coated onto the chip surface (4500 rpm for 2 minutes).

The waveguide chip was mounted on a stage equipped with a Peltier element and a thermistor. A temperature controller (ThorLabs Pro8000) regulated the temperature of the chip within 1 mK. Light from an ytterbium fiber laser (IPG Photonics, 1070 nm, TE-polarization) was coupled into the waveguide

F.T. Dullo is with the Northern Research Institute, P.O. Box 6434 Forskningsparken, Tromsø, Norway (e-mail: firehun.tsige.dullo@norut.no). M. Ingvaldsen, J. Jágerská, S.K. Jacobsen and OG Hellesø are with the University of Tromsø, Norway.

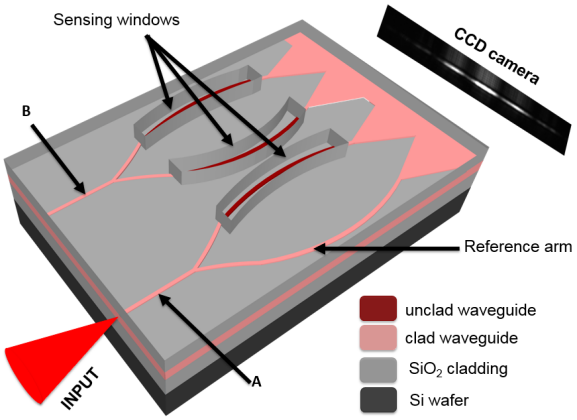

Fig. 1: Outline of the waveguide Young interferometers with one (A) and two (B) sensing windows, respectively. Interference fringes are shown at the output.

by a 20x objective lens. At the output, the interference fringes were collected by a 10x microscope objective and captured by a camera. The positions of the peaks of the fringes were recorded with a LabView program and analyzed to give the phase difference between the two arms. Further details on the design and the analysis of the fringes are given in [8].

III. Thermal Models

A. Thermo-optical model for uniform heating

The thermo-optical coefficient α_n for the layers (top-cladding, core and under-cladding) gives a change with temperature of the effective refractive index n_{eff} of the guided mode. As the two arms of the interferometer have the same length L and are fixed on a chip, thermal expansion and differences in length between the arms can be neglected. A mode-solver (Comsol 5.1) was used to find n_{eff} as a function of temperature, using the refractive indices and the thermo-optical coefficients given in Table I. The phase was calculated from:

$$\frac{\partial\varphi}{\partial T} = \frac{2\pi L}{\lambda_0}\frac{\partial n_{\text{eff}}}{\partial T} = \frac{2\pi L}{\lambda_0}\frac{n_{\text{eff}}(T+\Delta T) - n_{\text{eff}}(T)}{\Delta T}, \qquad (1)$$

with wavelength in vacuum λ_0, length of sensing window L and ΔT the temperature-step used. As the thermo-optical coefficients are small, n_{eff} was linear with ΔT. The difference in phase between the two arms becomes:

$$\Delta\varphi = \left(\frac{\partial\varphi}{\partial T}\right)_S \Delta T_S - \left(\frac{\partial\varphi}{\partial T}\right)_R \Delta T_R, \qquad (2)$$

with subscripts S and R representing the sensing and the reference arm, respectively. Different top-claddings on the two arms implies $\alpha_{nS} \neq \alpha_{nR}$ and $(\partial\varphi/\partial T)_S \neq (\partial\varphi/\partial T)_R$. Thus, uniform heating ($\Delta T_S = \Delta T_R$) will give a phase difference as function of temperature. This was investigated for air, oil and SAN using the Young interferometer with one sensing window (see Fig. 1), with silica on the reference arm. For a perfectly symmetric interferometer with the same materials on both arms, thus $(\partial\varphi/\partial T)_S = (\partial\varphi/\partial T)_R$, there is no phase difference for uniform heating.

TABLE I: Refractive indices and thermo-optical coefficients.

Material	n	$\alpha_n(10^{-6}/\text{K})$	Ref.
Air	1.00	-0.86	[9]
SiO_2	1.46	12.9	[10]
Oil	1.47	-371	Spec.
SAN	1.56	-110	[11]
Si_3N_4	2.0	24.5	[12]

B. Thermal model for asymmetric heating

Thermal simulations of the waveguides and the chip were also performed using Comsol. The two-dimensional model is shown in Fig. 2. It consists of an aluminium block at the bottom, silicon substrate (500 µm thick), silica under-cladding (2 or 10 µm thick), waveguide layer (150 nm thick) and air on top. The rib-height of 5 nm was not resolved in the simulation model as it is too small to affect the thermal behavior. To study the effect of asymmetric heating, a fast thermal shock (1 K at t = .1 s, rise-time 0.01 s) was applied for dynamic simulations, while constant 1 K heating was applied for stationary simulations. The heating was applied to the left of the waveguides; on the bottom (T_1) or on top of the chip (T_2 and T_3). Heating-region T_2 has a fixed width of 100µm and starts from the inner edge of the left waveguide, giving maximum asymmetry. The width of T_3 is set equal to the separation between the waveguides and starts in the centre between the waveguides, resembling a microfluidic channel centered on the left waveguide. For heating below (T_1), the bottom of the substrate and the top of the waveguide-layer were set to be isolating, while for heating above (T_2 and T_3), semi-infinite air and aluminium domains were included, as shown in Fig. 2. In both cases, the model had infinite domains on the left and the right side, as the chip is significantly wider (25 mm) than the region simulated (500 µm).

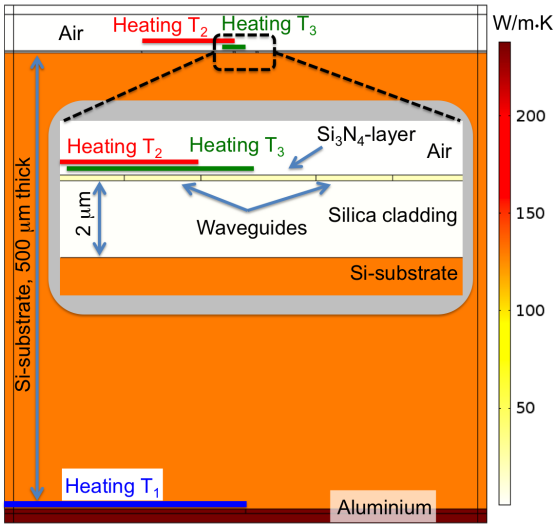

Fig. 2: Diagram of the thermal model showing the thermal conductivity of the materials. The insert zooms in on the waveguides and the 150 nm thick Si_3N_4 waveguide-layer.

IV. Results and Discussion

Temperature steps were applied to the chip and the phase measured as function of time at the output of the Young interferometers. Fig. 3 shows the results for a Young interferometer with a single sensing window covered with oil. The phase closely follows the temperature, even when there is a temperature overshoot. For large temperature steps, see circled areas, the phase is not perfectly linear with temperature. This might be due to mechanical movement of the chip caused by the large temperature steps. Similar measurements were done with SAN and air, as shown in Table II. The results show good agreement with the theoretical values found using Eq. (1) and (2). For air on the sensing arm, the thermal dependency is almost the same as that of the reference arm covered with silica. This combination thus gives an athermal device. The measurement for air was repeated several times, with a variation on the order of 10^{-3}. However, the measured value is similar to dependencies and noise found with symmetric interferometers (next paragraph), and thus also to the absolute error of the method.

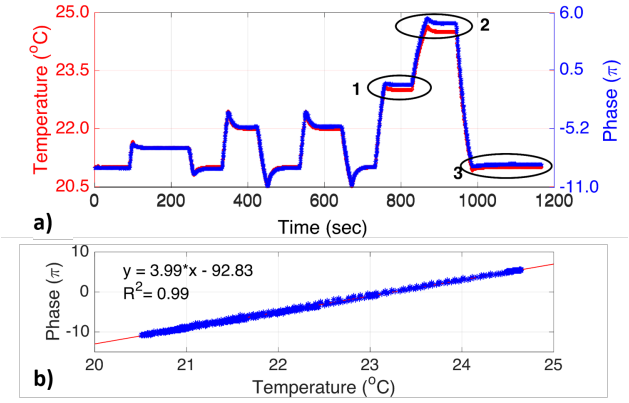

Fig. 3: Applied temperature and measured phase with one sensing window covered with oil a) as function of time and b) phase vs. applied temperature. Circles 1, 2 and 3 indicate slight deviations from linearity between temperature and phase.

For a symmetric interferometer, with two sensing windows covered with the same material, the phase should be independent of (uniform) temperature changes according to Eq. (2). This was tested by applying temperature steps in the same way as for a single sensing window. The result is shown in Fig. 4 with both windows covered with oil. The time-dependency (Fig. 4a) of the phase follows that of the temperature. The fitted line (Fig. 4b) has a slope of 0.06 π/K, which is two orders of magnitude smaller than for an interferometer with one sensing window covered by oil (see Table 2). The slope corresponds to a movement of the interference fringes with -3.8 pixels/K on the camera, and similar measurements with SAN and air on the two sensing windows gave slopes of -2.4 and -3.6 pixels/K, respectively. Repeating the experiment with a straight waveguide, i.e. no interferometer, gave a similar movement of the output beam with temperature, with a slope of -2.2 pixels/K. As the Young interferometer separates changes in phase from changes in amplitude, the measured phase does not depend on

TABLE II: Phase change with temperature for various top-claddings on a single waveguide and on an interferometer, both 20 mm long.

Single w.g.		Interferometer		
Cladding sens. arm	Theory (π/K)	Cladding ref. arm	Theory (π/K)	Measured (π/K)
SiO_2	0.73	-	-	-
Oil	-3.17	SiO_2	-3.90	-3.99
SAN	-1.01	SiO_2	-1.74	-1.81
Air	0.70	SiO_2	-0.034	-0.043

the input coupling or vertical movement of the chip. However, a sideways movement of the chip with temperature, will move the fringes horizontally in the same way as a change in phase. As the movement with temperature was approximately equal for the three interferometer measurements and for the straight waveguide, at 4 pixels/K or less, we conclude that this temperature dependency is due to mechanical movement of our set-up with temperature. Experimentally, a temperature dependency of the phase was thus not found, as expected for uniform temperature across the bottom of the chip.

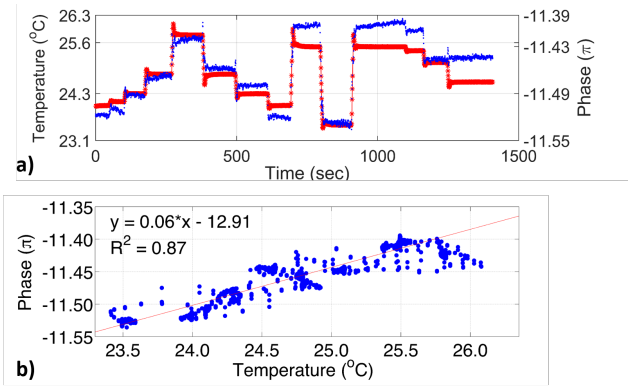

Fig. 4: Applied temperature and measured phase with both sensing windows covered with oil a) as function of time and b) phase vs. applied temperature.

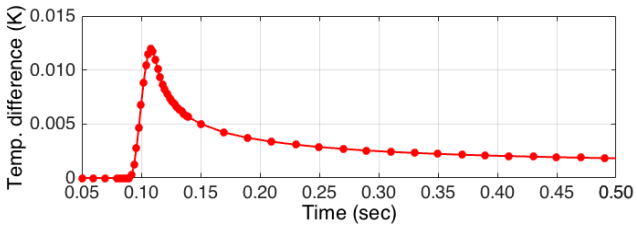

Fig. 5: Simulated transient temperature difference between the two waveguides when a 1 K step T_1 is applied on the lower left side of the substrate.

To study asymmetric heating of a symmetric interferometer, the thermal distribution was simulated with a 1 K temperature-step applied below the left part of the substrate (T_1 in Fig. 2). The resulting temperature difference between the left and the right waveguide is shown in Fig. 5. The transient difference in temperature reaches approximately 14 mK and decays to 1 mK after 1 sec. The peak value depends on the rise-time

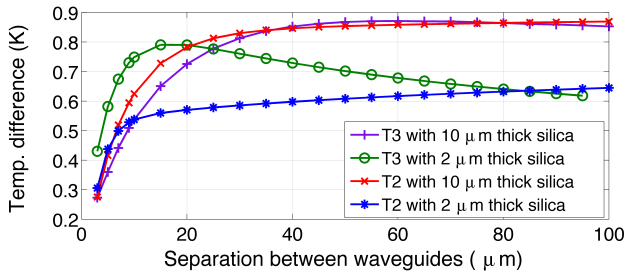

Fig. 6: Simulated, stationary temperature difference between the two waveguides with 1 K asymmetric heating of the surface. Heating regions T_2 and T_3 are defined in Fig. 2.

of the applied temperature-step (here: 0.01 s), while the fast decay is caused by the good thermal conductivity of the silicon substrate. For a more realistic temperature difference, with rise-time of several seconds and less asymmetric, the temperature difference will be well below 1 mK.

For a 1 K temperature step applied above the left waveguide (T_2), a time-dependent simulation showed that the temperature difference was within 10% of the stationary value within 1 sec. For heating of the top surface, stationary simulations were thus done, as shown in Fig. 6. The result depends on the separation between the two waveguides and the thickness of the silica layer. In addition, it depends on the width and position of the heated region (T_2 or T_3). The effect of asymmetric heating of the top surface is generally large, typically giving 0.5-0.9 K temperature difference for 1 K asymmetric heating. This is due to the thermally isolating silica layer and the thin Si_3N_4-layer, resulting in poor lateral heat conduction. The temperature difference decreases for separations of less than 10 µm. However, as the waveguides are 2 µm wide, there will be optical coupling between the waveguides before this difference is reduced significantly, e.g. by a factor 10. If the heating is caused by a microfluidic channel centered on one of the waveguides, case T_3 shows that it is an advantage to use a rather large separation and large microfluidic channel. Comparing heating above the chip (cases T_2 and T_3) with heating below the chip (case T_1), it is apparent that the device is almost insensitive to temperature instabilities below the chip, while it is sensitive to any asymmetric heating above the chip. Table II gives the temperature sensitivity for a single 20 mm long waveguide to be approximately $(\pm)1\pi/\mathrm{K}$ with air, silica or SAN as top-cladding. Therefore, the temperature difference between two arms with identical cladding must be less than 5 mK to bring the temperature-induced fluctuations down to 0.005π, which was the noise level for constant chip-temperature in this work.

V. Conclusion

The phase change as function of temperature was measured with a Young interferometer with a single sensing window and silica on the reference arm. The values were large and close to the simulated values for oil and SAN. For air and silica on the two arms, the temperature dependency is small and the measured value is close to the detection limit. A polymer, e.g. SAN, with a large thermo-optical coefficient on the sensing arm, can thus be used for on-chip temperature sensing, while if using this combination for biological or chemical sensing, the temperature of the device has to be very well stabilized. Air on the sensing arm gives athermal behaviour, but the large step in refractive index gives low homogeneous sensitivity to biological or chemical changes.

The symmetric device (with two sensing windows) is insensitive to hotspots or temperature steps applied to the bottom of the substrate, while it is very sensitive to asymmetric heating of the top surface. These two effects are expected because of, respectively, the excellent thermal conductivity of the substrate and the thermally isolating silica cladding. The effect of asymmetric heating of the top surface cannot be reduced significantly by reducing the separation between the waveguides. Thus, the temperature on the surface must be kept uniform to within a few mK, e.g. with microfluidic channels heating both sensing arms, and with almost identical materials on the two arms.

Acknowledgment

This work was supported by the Research Council of Norway. The authors would like to acknowledge the assistance of Viktor Sokolov, Cyprien Chauvet and Robin Chatel.

References

[1] A. L. Washburn and R. C. Bailey, "Photonics-on-a-chip: recent advances in integrated waveguides as enabling detection elements for real-world, lab-on-a-chip biosensing applications," *Analyst*, vol. 136, no. 2, pp. 227–236, 2011.

[2] P. Kozma, F. Kehl, E. Ehrentreich-Förster, C. Stamm, and F. F. Bier, "Integrated planar optical waveguide interferometer biosensors: A comparative review," *Biosensors and Bioelectronics*, vol. 58, pp. 287–307, 2014.

[3] B. Guha, A. Gondarenko, and M. Lipson, "Minimizing temperature sensitivity of silicon Mach-Zehnder interferometers," *Opt. Exp.*, vol. 18, no. 3, pp. 1879–1887, 2010.

[4] X. Tu, J. Song, T.-Y. Liow, M. K. Park, J. Q. Yiying, J. S. Kee, M. Yu, and G.-Q. Lo, "Thermal independent silicon-nitride slot waveguide biosensor with high sensitivity," *Opt. Exp.*, vol. 20, no. 3, pp. 2640–2648, 2012.

[5] I. S. Duport, P. Benech, and R. Rimet, "New integrated-optics interferometer in planar technology," *Appl. Opt.*, vol. 33, no. 25, pp. 5954–5958, 1994.

[6] S. Lindecrantz, J.-C. Tinguely, B. S. Ahluwalia, and O. Hellesø, "Characterization of a waveguide Mach-Zehnder interferometer using PDMS as a cover layer," *JEOS-RP*, vol. 10, 2015.

[7] F. Prieto, B. Sepulveda, A. Calle, A. Llobera, C. Domínguez, A. Abad, A. Montoya, and L. M. Lechuga, "An integrated optical interferometric nanodevice based on silicon technology for biosensor applications," *Nanotech.*, vol. 14, no. 8, p. 907, 2003.

[8] F. T. Dullo and O. G. Hellesø, "On-chip phase measurement for microparticles trapped on a waveguide," *LabChip*, vol. 15, no. 19, pp. 3918–3924, 2015.

[9] Ohara inc. [Online]. Available: http://www.ohara-inc.co.jp/en/product/optical/opticalglass/01002.html

[10] G. L. Klunder and R. E. Russo, "Core-based intrinsic fiber-optic absorption sensor for the detection of volatile organic compounds," *Appl. Spect.*, vol. 49, no. 3, pp. 379–385, 1995.

[11] N. Sultanova, S. Kasarova, and I. Nikolov, "Characteristics of optical polymers in the design of polymer and hybrid optical systems," *Bulg. J. Phys*, vol. 40, no. 3, pp. 258–264, 2013.

[12] A. Arbabi and L. L. Goddard, "Measurements of the refractive indices and thermo-optic coefficients of Si_3N_4 and SiO_x using microring resonances," *Opt. Lett.*, vol. 38, no. 19, pp. 3878–3881, 2013.

Bibliography

[1] W. S. Reeburgh. Global Methane Biogeochemistry. *Treatise on Geochemistry*, 4:65–89, 2003.

[2] IPCC. *Summary for Policymakers*, book section SPM, pages 1–30. Cambridge University Press, Cambridge, United Kingdom and New York, NY, USA, 2013.

[3] D. Amouroux, G. Roberts, S. Rapsomanikis, and M. O. Andreae. Biogenic Gas (CH4, N2O, DMS) Emission to the Atmosphere from Near-shore and Shelf Waters of the North-western Black Sea. *Estuarine, Coastal and Shelf Science*, 54(3):575–587, 2002.

[4] G. Rehder, R. W. Collier, K. Heeschen, P. M. Kosro, J. Barth, and E. Suess. Enhanced marine CH4 emissions to the atmosphere off Oregon caused by coastal upwelling. *Global Biogeochemical Cycles*, 16(3):2–11, 2002.

[5] E. J. Sauter, S. I. Muyakshin, J.-L. Charlou, M. Schlüter, A. Boetius, K. Jerosch, E. Damm, J.-P. Foucher, and M. Klages. Methane discharge from a deep-sea submarine mud volcano into the upper water column by gas hydrate-coated methane bubbles. *Earth and Planetary Science Letters*, 243(34):354–365, 2006.

[6] G. Myhre, D. Shindell, F.-M. Breon, W. Collins, J. Fuglestvedt, J. Huang, D. Koch, J.-F. Lamarque, D. Lee, B. Mendoza, T. Nakajima, A. Robock, G. Stephens, T. Takemura, and H. Zhang. *Anthropogenic and Natural Radiative Forcing*, book section 8, pages 659–740. Cambridge

University Press, Cambridge, United Kingdom and New York, NY, USA, 2013.

[7] K. A. Kvenvolden. Origins of Methane in the Earth Methane hydrate A major reservoir of carbon in the shallow geosphere? *Chemical Geology*, 71(1):41–51, 1988.

[8] F. T. Dullo, S. M. Lindecrantz, J Jágerská, J. H. Hansen, M. Engqvist, S. A. Solbø, and O. G. Hellesø. Sensitive on-chip methane detection with a cryptophane-A cladded Mach-Zehnder interferometer. *Opt. Express*, 23(24):31564–31573, nov 2015.

[9] R. W. Collier and M. D. Lilley. Composition of shelf methane seeps on the Cascadia Continental Margin. *Geophysical Research Letters*, 32(6), 2005.

[10] S. Kröger and R. J. Law. Sensing the sea. *Trends in Biotechnology*, 23(5):250–256, 2005.

[11] N. S. Lawrence. Analytical detection methodologies for methane and related hydrocarbons. *Talanta*, 69(2):385–392, 2006.

[12] J. Hodgkinson and R. P. Tatam. Optical gas sensing: a review. *Measurement Science and Technology*, 24(1):12004, 2013.

[13] J. Shemshad, S. M. Aminossadati, and M. S. Kizil. A review of developments in near infrared methane detection based on tunable diode laser. *Sensors and Actuators B: Chemical*, 171172:77–92, 2012.

[14] F. T. Dullo and O. G. Hellesø. On-chip phase measurement for microparticles trapped on a waveguide. *Lab Chip*, 15(19):3918–3924, 2015.

[15] C. Wagner, J. Frankenberger, and Peter P. Deimel. Optical pressure sensor based on a Mach-Zehnder interferometer integrated with a lateral a-Si:H p-i-n photodiode. *Photonics Technology Letters, IEEE*, 5(10):1257–1259, 1993.

[16] G. N. De Brabander, G. Beheim, and J. T. Boyd. Integrated optical micromachined pressure sensor with spectrally encoded output and temperature compensation. *Appl. Opt.*, 37(15):3264–3267, 1998.

[17] F. T. Dullo, M. Ingvaldsen, J. Jágerská, S. K. Jacobsen, and O. G. Hellesø. Temperature sensitivity of a waveguide Young interferometer. *Photonics Technology Letters, IEEE*, 2015.

[18] N. Fabricius, G. Gauglitz, and J. Ingenhoff. A gas sensor based on an integrated optical Mach-Zehnder interferometer. *Sensors and Actuators B: Chemical*, 7(13):672–676, 1992.

[19] C. Boulart, M. C. Mowlem, D. P. Connelly, J.-P. Dutasta, and C. R. German. A novel, low-cost, high performance dissolved methane sensor for aqueous environments. *Optics express*, 16(17):12607–12617, 2008.

[20] A Densmore, Xu D.-X., S Janz, P Waldron, J Lapointe, T Mischki, G Lopinski, A Delâge, J H Schmid, and P Cheben. Sensitive Label-Free Biomolecular Detection Using Thin Silicon Waveguides. *Advances in Optical Technologies*, 2008(725967):9 pages, 2008.

[21] P. Kozma, F. Kehl, E. Ehrentreich-Förster, C. Stamm, and F. F. Bier. Integrated planar optical waveguide interferometer biosensors: A comparative review. *Biosensors and Bioelectronics*, 58:287–307, 2014.

[22] A. L. Washburn and R. C. Bailey. Photonics-on-a-chip: recent advances in integrated waveguides as enabling detection elements for real-world{,} lab-on-a-chip biosensing applications. *Analyst*, 136(2):227–236, 2011.

[23] B. Guha, A. Gondarenko, and M. Lipson. Minimizing temperature sensitivity of silicon Mach-Zehnder interferometers. *Opt. Express*, 18(3):1879–1887, feb 2010.

[24] X. Tu, J. Song, T.-Y. Liow, M. K. Park, J. Q. Yiying, J. S. Kee, M. Yu, and G.-Q. Lo. Thermal independent Silicon-Nitride slot waveguide biosensor with high sensitivity. *Opt. Express*, 20(3):2640–2648, jan 2012.

[25] T. Brotin and J.-P. Dutasta. Cryptophanes and Their ComplexesPresent and Future. *Chemical Reviews*, 109(1):88–130, 2009.

[26] L. Garel, J.-P. Dutasta, and A. Collet. Complexation of Methane and Chlorofluorocarbons by Cryptophane-A in Organic Solution. *Angewandte Chemie International Edition in English*, 32(8):1169–1171, 1993.

[27] E. Souteyrand, D. Nicolas, J. R. Martin, J. P. Chauvet, and H. Perez. Behaviour of cryptophane molecules in gas media. *Sensors and Actuators B: Chemical*, 33(13):182–187, 1996.

[28] K. E. Chaffee, H. A. Fogarty, T. Brotin, B. M. Goodson, and J.-P. Dutasta. Encapsulation of Small Gas Molecules by Cryptophane-111 in Organic Solution. 1. Size- and Shape-Selective Complexation of Simple Hydrocarbons. *The Journal of Physical Chemistry A*, 113(49):13675–13684, 2009.

[29] M. Benounis, N. Jaffrezic-Renault, J.-P. Dutasta, K. Cherif, and A. Abdelghani. Study of a new evanescent wave optical fibre sensor for methane detection based on cryptophane molecules. *Sensors and Actuators B: Chemical*, 107(1):32–39, 2005.

[30] J. Yang, C. Tao, X. Li, G. Zhu, and W. Chen. Long-period fiber grating sensor with a styrene-acrylonitrile nano-film incorporating cryptophane A for methane detection. *Opt. Express*, 19(15):14696–14706, jul 2011.

[31] B. E. A. Saleh and M. C. Teich. *Fundamentals of Photonics*. Wiley-Interscience, Hoboken, N.J, 2 edition, 2007.

[32] I. S. Duport, P. Benech, and R. Rimet. New integrated-optics interferometer in planar technology. *Appl. Opt.*, 33(25):5954–5958, sep 1994.

[33] D. E. Aspnes. Localfield effects and effectivemedium theory: A microscopic perspective. *American Journal of Physics*, 50(8), 1982.

[34] J. C. Owens. Optical Refractive Index of Air : Dependence on Pressure , Temperature and Composition. 6(1), 1967.

[35] J. H. Gladstone and T. P. Dale. Researches on the Refraction, Dispersion, and Sensitiveness of Liquids. *Philosophical Transactions of the Royal Society of London*, 153:317–343, 1863.

[36] S. Maj. On the relationship between refractive index and density for SiO2 polymorphs. *Physics and Chemistry of Minerals*, 10(3):133–136, 1984.

[37] N. M. Balzaretti and J. A. H. da Jornada. Pressure dependence of the refractive index of diamond, cubic silicon carbide and cubic boron nitride. *Solid State Communications*, 99(12):943–948, 1996.

[38] H. R. Philipp. Silicon Dioxide (SiO2) (Glass). In Edward D Palik, editor, *Handbook of Optical Constants of Solids*, pages 749–763. Academic Press, Burlington, 1997.

[39] H. R. Philipp. Silicon Nitride (Si3N4) (Noncrystalline). In Edward D Palik, editor, *Handbook of Optical Constants of Solids*, pages 771–774. Academic Press, Burlington, 1997.

[40] G. L. Klunder and R. E. Russo. Core-Based Intrinsic Fiber-Optic Absorption Sensor for the Detection of Volatile Organic Compounds. *Appl. Spectrosc.*, 49(3):379–385, mar 1995.

[41] N. G. Sultanova, S. N. Kasarova, and I. D. Nikolov. Characterization of optical properties of optical polymers. *Optical and Quantum Electronics*, 45(3):221–232, 2013.

[42] A. Arbabi and L. L. Goddard. Measurements of the refractive indices and thermo-optic coefficients of Si3N4 and SiOx using microring resonances. *Opt. Lett.*, 38(19):3878–3881, 2013.

[43] S. M. Lindecrantz and O. G. Hellesø. Estimation of Propagation Losses for Narrow Strip and Rib Waveguides. *Photonics Technology Letters, IEEE*, 26(18):1836–1839, sep 2014.

[44] S. M. Lindecrantz, J.-C. Tinguely, B. S. Ahluwalia, and O. G. Hellesø. Characterization of a waveguide Mach-Zehnder interferometer using PDMS as a cover layer. *Journal of the European Optical Society - Rapid publications*, 10(0), 2015.

[45] F. Prieto, B. Sepúlveda, A. Calle, A. Llobera, C. Domínguez, A. Abad, A. Montoya, and L. M. Lechuga. An integrated optical interferometric nanodevice based on silicon technology for biosensor applications. *Nanotechnology*, 14(8):907, 2003.

[46] F. T. Dullo, J.-C. Tinguely, S. A. Solbø, and O. G. Hellesø. Single-Mode Limit and Bending Losses for Shallow Rib Si3N4 Waveguides. *Photonics Technology Letters, IEEE*, 7(1):1–11, feb 2015.

[47] P. Werle, R. Mücke, and F. Slemr. The limits of signal averaging in atmospheric trace-gas monitoring by tunable diode-laser absorption spectroscopy (TDLAS). *Applied Physics B Photophysics and Laser Chemistry*, 57(2):131–139, 1993.

[48] F. Wang and A. Adibi. Precision measurements for propagation properties of high-definition polymer waveguides by imaging of scattered light. 47(February 2008):2–5, 2012.

[49] Canada-France-Hawaii Telescope. Applying flat field and dark frame corrections. *http://www.cfht.hawaii.edu/~baril/Pyxis/Help/flatdarkfield.html*.

[50] D. W. Van Krevelen and K. T. Nijenhuis. Chapter 18 - Properties Determining Mass Transfer In Polymeric Systems. In D W Van KrevelenRevised By and K Te Nijenhuis, editors, *Properties of Polymers (Fourth Edition)*, pages 655–702. Elsevier, Amsterdam, fourth edi edition, 2009.

[51] V. M. Shah, B. J. Hardy, and S. A. Stern. Solubility of carbon dioxide, methane, and propane in silicone polymers: Effect of polymer side chains. *Journal of Polymer Science Part B: Polymer Physics*, 24(9):2033–2047, 1986.

[52] D. MacDougall and W. B. Crummett. Guidelines for data acquisition and data quality evaluation in environmental chemistry. *Analytical Chemistry*, 52(14):2242–2249, 1980.

[53] H.-P. Loock and P. D. Wentzell. Detection limits of chemical sensors: Applications and misapplications. *Sensors and Actuators B: Chemical*, 173:157–163, 2012.